The SICT/Plasma Tech/Tribology 2022 International Joint Conference

Hybrid event - Apr 27 to 29, 2022

Conference Proceedings

DOI:
https://doi.org/10.26799/cp-sict-plasmatech-tribology-2022

Proceedings of the SICT/PlasmaTech/Tribology 2022 Joint International Conference
Barcelona, Spain – April 27 – 29, 2022
DOI: https://doi.org/10.26799/cp-sict-plasmatech-tribology-2022

Triboscopic Insights into Long-Term Tribologic Behavior of Brass/ta-C in High Vacuum

Fabian Härtwig[1,2], Lars Lorenz[1,2], Stefan Makowski[2], Matthias Krause[3], and Andrés Fabián Lasagni[1,2]

[1]Institute of Manufacturing Science and Engineering, Technische Universität Dresden
George-Bähr-Str. 3c, Dresden, Germany, fabian.haertwig@iws.fraunhofer.de, lars.lorenz@tu-dresden.de, andres_fabian.lasagni@tu-dresden.de
[2]Fraunhofer Institute for Material and Beam Technology IWS
Winterbergstraße 28, Dresden, Germany, stefan.makowski@iws.fraunhofer.de
[3]Institute of Ion Beam Physics and Materials Research, Helmholtz-Zentrum Dresden-Rossendorf
Bautzner Landstraße 400, Dresden, Germany, matthias.krause@hzdr.de

Abstract

It is widely known that tribological systems operating in vacuum environments face significant challenges. MoS_2 is a well-known material for its low friction properties in both ambient and vacuum environments. However, it has a low wear resistance and a limited ability to withstand higher contact pressures. A possible alternative to MoS_2 are super-hard hydrogen-free tetrahedral amorphous carbon coatings (ta-C). In normal atmospheric conditions, they have low friction and wear properties, but their performance in vacuum is limited. In this work, ta-C coatings are paired with brass in high vacuum conditions. Long-term tribological performance tests are conducted and analyzed using triboscopic imaging. It was found that the brass/ta-C friction pair exhibited an increase of the friction coefficient in the long term (up to 0.52) due to a change in wear mechanism. Different wear and healing behaviors could be found for both the brass counterbody and the ta-C discs using triboscopy.

Keywords: diamond like coatings, DLC, ta-C, tribology, vacuum, brass, triboscopy

1. Introduction

Carbon can exist in two forms of covalently bonded crystal structures, each with its own bonding configuration and lattice structure. The carbon atoms in graphite are arranged in A-B stacked graphene planes (sp^2 carbon hybridization) in trigonal planar configuration. In diamond they are arranged in a tetrahedral configuration (sp^3 carbon hybridization) resulting in very high material strength and hardness in all dimensions [1]. Carbon coatings can be amorphous, containing a mix of both hybridization states. When primarily composed of sp^3-bonded C atoms, they are referred to as tetrahedral hydrogen-free amorphous carbon (ta-C) [1]. The coating is referred to as hydrogen-free amorphous carbon (a-C) when sp^2 bonds dominate [1]. Carbon coatings that also contain hydrogen are known as hydrogenated amorphous carbon films (a-C:H or ta-C:H) [1].

In particular, ta-C coatings have been shown to be very successful in reducing friction in non-lubricated contact as well as in ambient air [2, 3]. Furthermore, humidity, the mating material, and the amount and type of surface defects have shown to have an impact on the tribological behavior [3–5]. When the ambient humidity is very low, the friction performance decreases significantly. This is especially problematic in unlubricated high-vacuum applications [3–5]. Meunier et al. demonstrated in 2005 that ta-C coatings paired with 100Cr6 steel counterbodies show extremely high wear and a high coefficient of friction (COF) in vacuum conditions [6]. In a previous work, brass was found to be a promising wear partner with ta-C irrespective of pressure and humidity. Furthermore, in the long-term some unexplained irregular friction and wear patterns were found [3].

Triboscopy is a method of analyzing the friction data of tribological measurements revealing position and time of friction events. It was recently further developed and improved by Lorenz et al. [7].

The current study is the first systematic investigation of the effect of brass counterbodies on the friction properties of ta-C in a high vacuum using triboscopy. The measured data is investigated using triboscopic imaging.

DOI: https://doi.org/10.26799/cp-sict-plasmatech-tribology-2022

2. Materials and Methods

2.1 Coating Deposition

The ta-C coated steel discs (100Cr6/1.3505, hardened to 60 HRC, 24 mm diameter, Ra < 0.03 µm) were manufactured using a commercial physical vapor deposition (PVD) chamber (VTD Vakuumtechnik Dresden GmbH, Dresden, Germany) with a plasma-filtered, laser-ignited, pulsed vacuum-arc process [8]. The steel discs were etched with Ar+ ions using a hollow-cathode plasma source before deposition. A 100 nm chromium layer was then deposited using magnetron sputtering. While being coated, the substrates were rotated inside the PVD chamber with a two axis-planetary drive. Then, the ta-C was coated in the PVD chamber using the Laser-Arc carbon coating process. Finally, after deposition in order to achieve a mirror polish surface quality, all the ta-C coated discs were lapped with a diamond slurry.

The ball crater method was used to determine the coating thickness. The discs had an average coating thickness of (2.1 ± 0.2) µm. The Young's modulus and hardness of the coating were measured using a ZHN nanomechanical test system from Zwick/Roell (Ulm, Germany) using the quasi-continuous stiffness method (QCSM). Loads of up to 100 mN were applied using a Berkovich tip. The calculation was done as in EN ISO 14577-4:2016, with a sigmoid fit model for the extrapolation of the coating indentation modulus, as has been previously reported [9]. The Young´s modulus was then verified using surface acoustic wave spectroscopy [10]. The Young´s modulus as calculated from the QCSM measurement was (693 ± 18) GPa. The coatings' sp^3 content (F) was calculated using the formula F = E/800 GPa applicable for hydrogen-free amorphous carbon [11]. With the previously mentioned Young´s modulus (E) the sp^3 content could be estimated to be 86.6%. The 10 mm steel (G5) and bass (G200) counterbodies were ordered from TIS Wälzkörpertechnologie (Gauting, Germany).

2.2 Tribology and Characterization

A UHVT-14 ultra-high vacuum tribometer (Tetra Basalt, Ilmenau, Germany) working in a ball-on-disc arrangement was used. The tribometer was enclosed in a vacuum chamber that could reach pressures ranging from ambient to 10^{-9} mbar. The disc rotated at a sliding speed of 3 mm/s with a normal force of 5 N. Experiments were carried out using a sliding distance of 54.0 and 67.5 meters. The measured pressure was between 1 and 4×10^{-7} mbar ("high vacuum"). The terminology [counterbody]/[disc] is used to label tribopairs in this work.

By averaging the recorded friction coefficient values from the last 5 m of equivalent sliding distance, the coefficient of friction (COF) was calculated. Triboscopic images were generated from raw friction data as detailed in a recent paper by Lorenz et al. [7].

3. Results and Discussion

Two experiments were performed using the brass/ta-C system in high vacuum conditions. Considerable friction coefficient degradation could be seen in the experiment performed with a distance of 67.5 m. The COF came to 0.52. In the experiment performed with a sliding distance of 54.0 m, some friction fluctuations were observed, but the COF remained very low overall (0.08). Overall, the ta-C/brass pairing does not seem to be stable for extended sliding lengths.

Figure 1a shows the triboscopic image of the experiment performed with a sliding distance of 67.5 m [7]. The friction coefficient is shown time resolved and plotted as a function of the counterbody position. The friction intensity is color coded. At the bottom of the image, a normal friction plot over time is shown and to the right the consolidated friction plot depending on counterbody position is visible. Multiple insights can be gained from the triboscopic image. Firstly, the steep friction drops which are visible in the normal friction diagram (bottom) can also be seen clearly in the triboscopic imagery. It is revealed that the friction dropped uniformly and to similar levels at all positions on the disc over multiple cycles. Therefore, the steep friction drops were not caused by localized "healing" of the coating but must be correlated with some changes of the brass counterbody wear scar. This change only lasted for a small number of cycles, then at all disc positions the friction coefficient returns to similar values as before the low friction event. This indicates that the change in the friction mechanism occurs on the counterbody surface, and not at the disc. Temporarily the counterbody seems to be passivated. We hypothesize the passivation mechanism is caused by the transfer of ta-C debris from the coating to the counter body.

DOI: https://doi.org/10.26799/cp-sict-plasmatech-tribology-2022

Secondly, in the triboscopic image different friction zones are visible denoted by the dissimilar COFs. These zones do not seem to change position over the course of the experiment. However, some of these regions with high COF were able to "heal", for example at the position between 190 and 360° from cycle 200 to 400. At other disc positions the friction coefficient remained below ≈0.3 for the whole experiment (90-110°). At again other positions, the friction coefficient always remained higher than ≈0.5 (30-90°). The transition between these zones was abrupt, mostly positionally consistent and clearly visible in the triboscopic image. We hypothesize, that brass is being deposited onto the disc in different amounts at various positions. At high deposition positions the COF rises because of brass counterbody to brass wear particle cold welding.

(**a**)

(**b**)

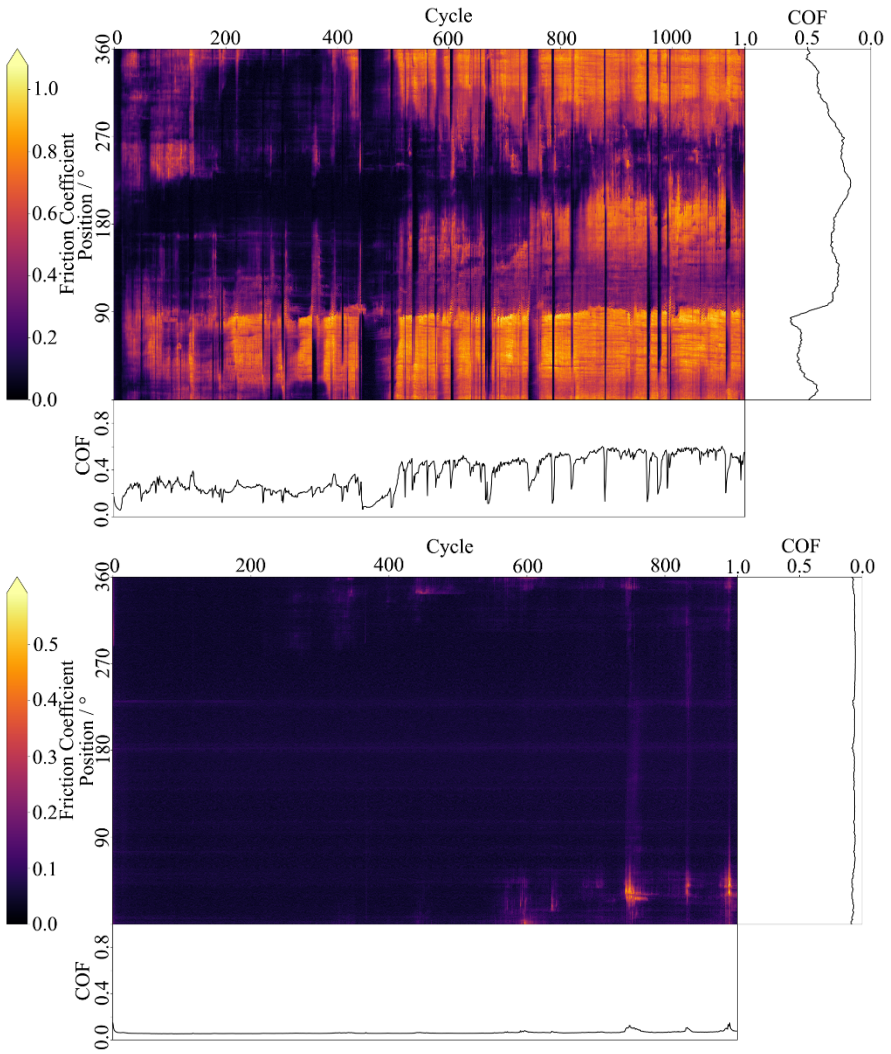

Fig. 1: Triboscopic images of experiments performed at sliding distances of (**a**) 67.5 m and (**b**) 54.0 m (brass/ta-C system) in high vacuum. The main plot in the middle represents friction depending on time (X-Axis) and position (Y-Axis) of counterbody on disc. The COF is shown according to a color chart (left). The plots at the right represent consolidated friction depending on counterbody position. Bottom diagram shows normal friction coefficient in relation to cycle number (time). Modified from [7]

In Figure 1b, the triboscopic image of the experiment corresponding to a sliding distance of 54.0 m is shown. In the bottom friction diagram some instability spikes can be seen. This can be seen more clearly in the triboscopic image. The friction instability originates only in a small area of the disc (0-60°). Friction peaks up to 0.5 could be seen multiple times. However, they were "healed" within 10 to 30 cycles. The coating did not seem to "heal" completely though, since all the friction spikes happened in the same area (0-60°), while the entire rest of the track remained at very low friction. This increase in friction again originates from the transfer of brass onto the wear track and the subsequent high-friction brass/brass contact [7]. After the transferred brass is moved out of the wear track, the original low friction brass/ta-C contact is restored.

DOI: https://doi.org/10.26799/cp-sict-plasmatech-tribology-2022

4. Conclusion

Brass counterbodies were tested against ta-C coatings under high vacuum conditions (1 to 4 × 10^{-7} mbar) in tribological sliding experiments. Long-term experiments were performed with sliding distances of 54.0 m and 67.5 m (COF = 0.08 and 0.52). In one experiment a strong friction instability, as well as a high long-term friction coefficient was found. Using triboscopic analysis, it could be shown that the wear mechanism for the studied system is complex and often the sum of tribo-mechanisms on both sides of the contact. In the experiments the transition from low to high friction developed randomly and abruptly, which has been attributed to the transfer of brass to the wear track. Further, a multitude of different "healing" behaviors of both the counterbody as well as the coating were discovered. Since these features are not identifiable with conventional friction curves, the obtained triboscopic images proved to be very useful in determining the origin of friction increase, as well as giving inferences about the counterbody and disc effects separately. In the future the use of this method may be expanded by further analyzing interesting wear track positions with methods such as Raman spectroscopy or RBS. Overall, the studied brass/ta-C system was found to be a possible solution for achieving low friction in vacuum if the long-term change in friction mechanism of the brass counterbody can be prevented or controlled.

Acknowledgements

This work was supported by the Deutsche Forschungsgemeinschaft (DFG – German Research Foundation) under grant agreement 415726702 and Sächsische Aufbaubank (SAB) within project LUBRICOAT.

References

1. *ISO 20523:2017 Carbon based films - Classification and designations*, 20523, International Organization for Standardization, Genf, Sep. 2017. [Online]. Available: https://www.iso.org/standard/68243.html
2. V. Weihnacht, A. Brückner, and S. Bräunling, "ta-C beschichtete Werkzeuge für die Trockenumformung von Aluminiumblechen," *VIP*, vol. 20, no. 3, pp. 6–10, 2008, doi: 10.1002/vipr.200800356.
3. F. Härtwig, L. Lorenz, S. Makowski, M. Krause, C. Habenicht, and A. F. Lasagni, "Low-Friction of ta-C Coatings Paired with Brass and Other Materials under Vacuum and Atmospheric Conditions," *Materials (Basel, Switzerland)*, vol. 15, no. 7, p. 2534, 2022, doi: 10.3390/ma15072534.
4. V. Weihnacht, S. Makowski, A. Brückner, G. Theiler, and T. Gradt, "Tribologie und Anwendung trocken laufender ta-C-Schichten," (in deu), *Tribologie und Schmierungstechnik*, vol. 59, no. 6, pp. 41–44, 2012. [Online]. Available: https://opus4.kobv.de/opus4-bam/frontdoor/index/index/docId/28004
5. J. Andersson, R.A. Erck, and A. Erdemir, "Frictional behavior of diamondlike carbon films in vacuum and under varying water vapor pressure," *Surface and Coatings Technology*, 163-164, no. 4, pp. 535–540, 2003, doi: 10.1016/S0257-8972(02)00617-5.
6. C. Meunier, P. Alers, L. Marot, J. Stauffer, N. Randall, and S. Mikhailov, "Friction properties of ta-C and a-C:H coatings under high vacuum," *Surface and Coatings Technology*, vol. 200, 5-6, pp. 1976–1981, 2005, doi: 10.1016/j.surfcoat.2005.08.013.
7. L. Lorenz, S. Makowski, V. Weihnacht, and Á. F. Lasagni, "Advantages of Using Triboscopic Imaging: Case Studies on Carbon Coatings in Non-Lubricated Friction Conditions.," *[Manuscript submitted for publication]*, 2022.
8. F. Kaulfuss *et al.,* "Effect of Energy and Temperature on Tetrahedral Amorphous Carbon Coatings Deposited by Filtered Laser-Arc," *Materials (Basel, Switzerland)*, vol. 14, no. 9, p. 2176, 2021, doi: 10.3390/ma14092176.
9. L. Lorenz, T. Chudoba, S. Makowski, M. Zawischa, F. Schaller, and V. Weihnacht, "Indentation modulus extrapolation and thickness estimation of ta-C coatings from nanoindentation," *J Mater Sci*, pp. 1–9, 2021, doi: 10.1007/s10853-021-06448-2.
10. D. Schneider, T. Schwarz, H. Scheibe, and M. Panzner, "Non-destructive evaluation of diamond and diamond-like carbon films by laser induced surface acoustic waves," 1997. [Online]. Available: https://www.semanticscholar.org/paper/Non-destructive-evaluation-of-diamond-and-carbon-by-Schneider-Schwarz/9c29bd9b93cb9226d0481238e6a32975d12155bc
11. B. Schultrich, *Tetrahedrally Bonded Amorphous Carbon Films I: Basics, Structure and Preparation*. Berlin, Heidelberg: Springer Berlin Heidelberg, 2018.

Proceedings of the SICT/PlasmaTech/Tribology 2022 Joint International Conference
Barcelona, Spain – April 27 – 29, 2022
DOI: https://doi.org/10.26799/cp-sict-plasmatech-tribology-2022

Tribological Performance of 2D Nano-coated Steel Surfaces

M.J.G. Guimarey[1,2,*], M. Hadfield[1], A. Abdelkader[1]

[1]Department of Design and Engineering, Bournemouth University, Talbot Campus, Poole, United Kingdom
[2]Nafomat Group, Department of Applied Physics, iMATUS, University of Santiago de Compostela, Santiago de Compostela, Spain
*mgarciaguimarey@bournemouth.ac.uk

Abstract

Herein we introduce a multifunctional coating based on two-dimensional (2D) materials deposited on mild steel by a spray coating method combined with post-heat treatment at low temperature. We have investigated three different coating films composed of 2D hexagonal boron nitride (h-BN), graphene nanoplatelets (GNP), and a heterogeneous structure of both nanomaterials (h-BN/GNP). The mechanical and tribological (friction and wear) properties of the coatings compared with bare steel were performed and analysed using a Vickers micro-hardness testing, ball-on-plate tribometer, and 3D optical profilometer, respectively. The frictional tests were performed in dry and lubricated conditions, using a formulated commercial oil, 5W-30, as a lubricant. The results indicated that the coating enhances the resistance to friction and wear as well as the hardness of the steel surface. In friction tests with sliding steel-steel tribo-pairs under dry conditions, graphene-containing ethanol solution coating decreased the coefficient of friction and wear area by 21% and 31%, respectively. Interestingly, it is revealed that under dry and lubricated conditions, graphene-doped h-BN exhibits outstanding anti-wear properties synergistically compared to stand-alone 2D materials.

Keywords: Graphene Nanoplatelets; Hexagonal Boron Nitride; Coating; Hardness; Friction; Wear.

1. Introduction

Improving operating efficiency, reducing emissions, and maximising uptime and reliability of mechanical systems are major industrial endeavours [1]. One specific strategy to improve efficiency and reduce energy consumption is based on developing wear-resistant and low-friction coatings for sliding components. The synergy between nanomaterials and lubricants has shown great promise in addressing this challenge with reported excellent friction and wear performance [2]. However, liquid lubricants may not be used under certain operating conditions or applications (e.g. high temperature or vacuum). Therefore, researchers have pointed out the numerous advantages of surface modification using nanoparticles for this purpose [3]. Several materials have been examined as the basis for tribological coatings, including titanium, tungsten, boron, and carbon materials [4]. Owing to their tiny size, nanoparticles can be incorporated into surface imperfections, enhancing their lubricating properties, preventing corrosion, reducing friction, and improving wear resistance. At the same time, due to the influence of surface effect and small size effect, nanomaterials have many distinctive characteristics from macromaterials in terms of physical and mechanical properties, such as high strength, high toughness, and high specific heat, high thermal expansion rate and high conductivity. Numerous articles have shown the effectiveness of adding nanoparticles to the surface by employing different preparation methods of surface coatings and types of nano-coating materials.

This work investigates the influence of various 2D materials (h-BN and GNP) and their heterogeneous mixture (h-BN/GNP) as surface modifiers on mild steel surfaces. The experimental results showed that the heterogeneous structure h-BN/GNP nanomaterial has better effects on enhancing the wear resistance than pristine graphene or hBN both in dry and lubricated conditions. For instance, during dry frictional tests under 5 N of load, the wear area reduced by 44%, and the coefficient of friction reduced by 18%.

2. Material and methods

The scheme of the experimental procedure, including surface coatings on mild steel, is shown in Fig. 1. Firstly, the mild steel surfaces were ground using water-based sandpaper and polished with polycrystalline diamond suspension. After polishing, the samples were spray-coated with GNP, h-BN and h-BN/GNP suspensions sonicated in distilled water/ethanol (1:1) for 24 hours. 200 layers of each nanomaterial were applied to the samples. The uncoated and coated steel substrates were then heat-treated in a tube furnace under an Ar

DOI: https://doi.org/10.26799/cp-sict-plasmatech-tribology-2022

atmosphere at different temperatures (200, 300 and 400°C). This two-step surface coating method is illustrated in Fig. 2. A Buehler hardness tester was used for the hardness tests (Fig. 1), and at least five replicates were performed on each sample. The optimum conditions of heating time and temperature were determined based on the hardness results. Reciprocating sliding frictional tests of uncoated and coated mild steel flat substrates against chrome steel balls were performed at room temperature using a CSM tribometer with a ball-on-plate contact geometry. The acquisition parameters are gathered in Fig. 1. The wear scars produced on the substrates by the friction tests were analysed with a Sensofar S Neox 3D optical profilometer. Wear dimensions (wear track width, WTW and area) were evaluated in three different zones for each worn track to obtain average values. In addition, the roughness (Ra) of the abraded substrates was determined according to ISO4287 (Gaussian filter with a cut-off wavelength of 0.08 mm). Roughness values are averages of at least three measurements.

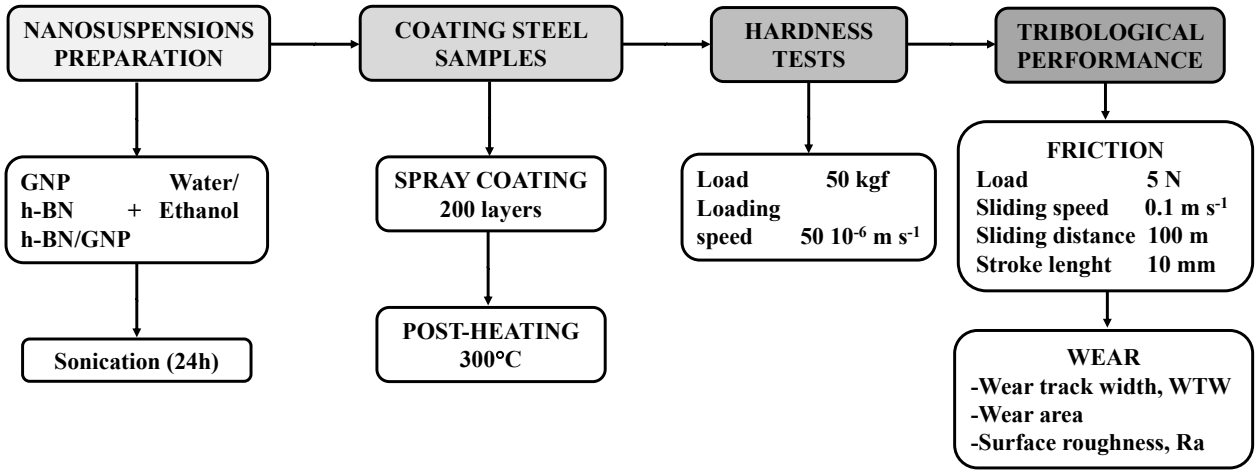

Fig. 1: Scheme of the experimental procedure carried out in this work.

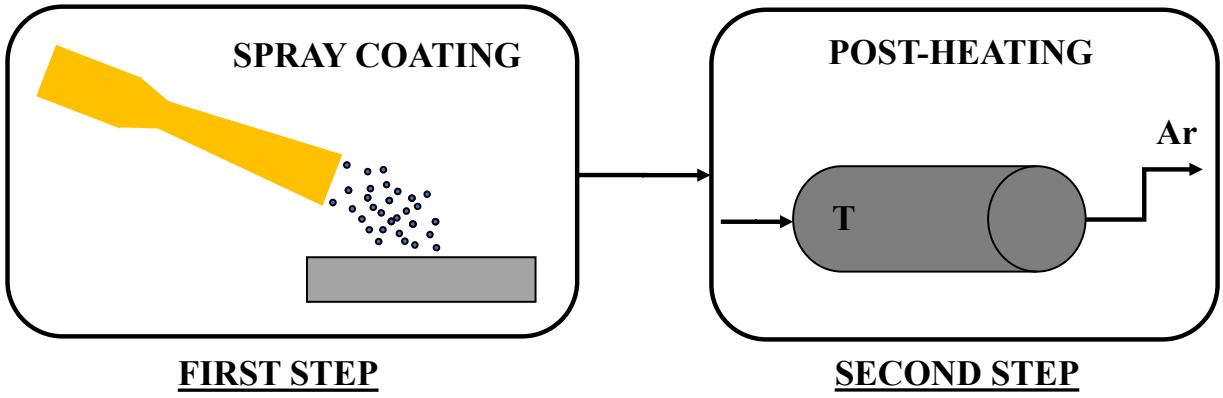

Fig. 2: Surface coatings method on mild steel.

3. Results and discussions

The greatest improvement in the hardness was observed for the steel coated with a post-heat treatment at 300°C. An increase of 2.5, 3.3 and 2.6 % could be achieved for the 200-layer GNP, h-BN and h-BN/GNP coatings compared to the uncoated steel substrate, respectively (Fig. 3).

DOI: https://doi.org/10.26799/cp-sict-plasmatech-tribology-2022

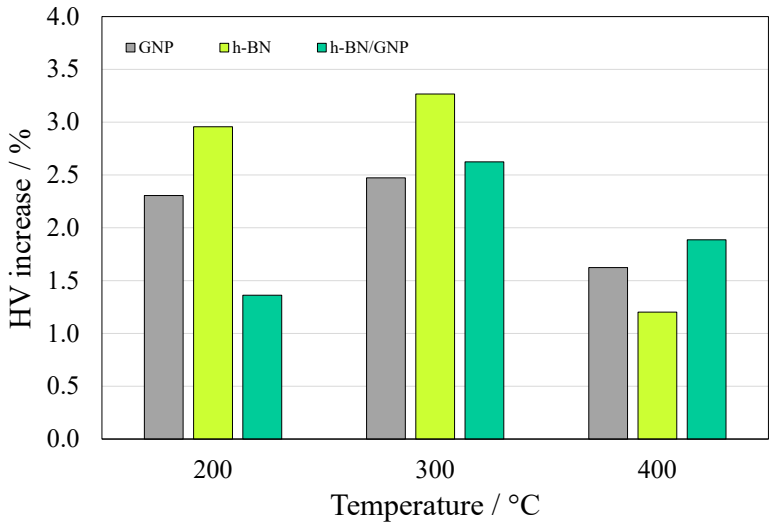

Fig. 3: Increase in Vickers hardness of steel substrates coated with 200 layers of different 2D materials at different temperatures.

Sliding friction tests were performed on substrates uncoated and coated with 200 layers of each nanomaterial (GNP, h-BN and h-BN/GNP) and post-heated to 300°C for 4h first in dry conditions and then using a commercial oil as a lubricant (5W-30). For dry lubrication conditions, excellent anti-friction behaviour is revealed for all coated samples compared to the bare one, reaching a coefficient of friction (COF) reduction of 22% for the steel sample coated with 200 layers of h-BN. This is not the case when an oil (5W-30) is used as a lubricant between the contact surfaces during sliding friction tests. Only the GNP-coated substrate produces a 15% improvement in COF over the bare sample; the h-BN and hybrid coatings do not achieve this anti-friction effect when 5W-30 lubricant is used.

After the friction tests, the wear scars produced on the substrates were optically analysed. Thus, excellent anti-wear performance was revealed for the nano-additive based coated substrates. Particularly for the h-BN/GNP based hybrid coating, a 57% and 44% reduction in wear area could be observed with and without lubricant, respectively. The observed reduction in the wear area for the GNP and h-BN coatings is 31% and 28% when no lubricant is used compared to bare steel samples, respectively (Fig. 4).

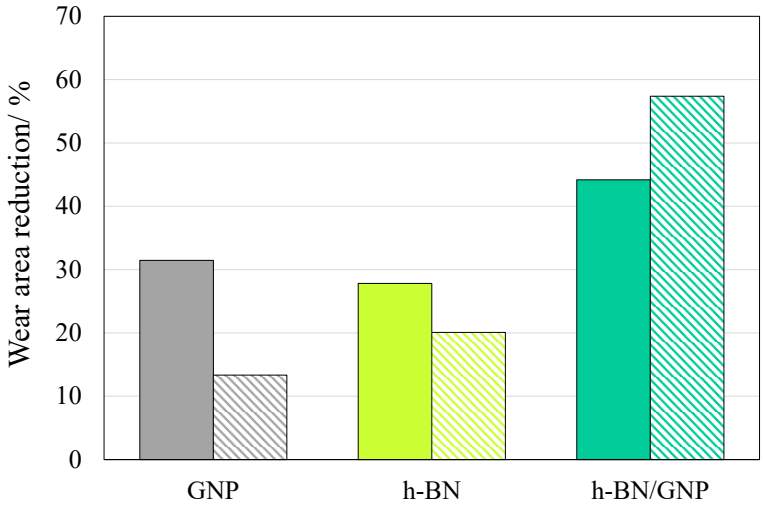

Fig. 4: Wear cross-sectional area for uncoated and coated substrates in two different lubrication conditions: dry (filled bar) and lubricated (grated bar).

Since the wear mechanism is strongly dependent on the surface roughness [5], the roughness (Ra) of the worn tracks was also measured and presented in Table 1. Lower roughness after friction tests was obtained for the surfaces lubricated with 5W-30 engine oil than those without lubricant. Precisely, a Ra value of 170 nm was

DOI: https://doi.org/10.26799/cp-sict-plasmatech-tribology-2022

obtained for the uncoated steel under dry conditions, reduced to 56 nm when the lubricant was used (three times lower). Furthermore, for the engine oil lubricated friction tests, it is observed that the roughness decreases by 26%, 48% and 36% for the GNP, h-BN and h-BN/GNP coated substrates with respect to the uncoated substrate, respectively. As a result, it can be concluded that a polishing effect occurs due to the presence of the 2D materials nano-additives [6].

Table 1: Average surface roughness (Ra) and its standard deviation (σ) for the uncoated and coated substrates.

	Ra /nm	σ /nm	Ra /nm	σ /nm
Substrate	DRY		LUBRICATED	
Uncoated Mild Steel	170	23.8	55.6	4.11
GNP	146	17.7	41.4	2.27
h-BN	169	24.5	28.7	1.29
h-BN/GNP	165	23.6	35.6	1.11

4. Conclusion

Increasing demand for the tribological properties of many mechanical systems requires new designs and improvements in surface modifications. Nanoparticles exhibiting many unique mechanical properties have become one of the most attractive choices for meeting these needs in recent years. In this work, surface coatings were successfully developed by spraying GNP and h-BN, and a heterogeneous mixture of both nano-additives in mild steel substrates. The optimum conditions for the hardening process of the 2D nanomaterials coated mild steel surface were 300°C for 4 h. The novel manufactured surface nano-coating showed excellent wear resistance characteristics. These nano-coatings revealed a wear area decrease under dry conditions of almost 31, 28, and 44% for 200 layers GNP, h-BN, and h-BN/ GNP, respectively, compared to bare mild steel. This research suggests that this sort of nano-coating has the potential to improve the tribological performance of steel-steel tribo-pairs under dry and lubricated conditions.

Acknowledgements

Spanish Ministry of Economy and Competitiveness and the Xunta de Galicia have supported this work through, GRC ED431C 2020/10 and PID2020-112846RB-C22 projects. Dr. María J. G. Guimarey acknowledges a postdoctoral fellowship (ED481B-2019-015) from the Xunta de Galicia (Spain) and the Jost Foundation for the travel fund to participate in the Tribology 2022 International Conference.

References

1. K. Holmberg, P. Kivikytö-Reponen, P. Härkisaari, K. Valtonen, A. Erdemir, “Global energy consumption due to friction and wear in the mining industry”, *Tribol. Int.*, vol. 115, pp. 116-139, 2017.
2. M.J.G. Guimarey, A. Abdelkader, M.J.P. Comuñas, C. Alvarez-Lorenzo, B. Thomas, J. Fernandez, M. Hadfield, “Comparison between thermophysical and tribological properties of two engine lubricant additives: electrochemically exfoliated graphene and molybdenum disulfide nanoplatelets”, *Nanotechnol.*, vol. 32, pp. 025701-025714, 2021.
3. T.W. Scharf, S.V. Prasad, “Solid lubricants: a review”, *J. Mater. Sci.*, vol. 48, pp. 511–531, 2013.
4. K. Holmberg and A. Matthews, *Coatings tribology: properties, mechanisms, techniques and applications in surface engineering*. Amsterdam: Elsevier, 2009.
5. R. Gheisari, K. Bashandeh, A.A. Polycarpou, “Effect of surface polishing on the tribological performance of hard coatings under lubricated three-body abrasive conditions”, *Surf. Topogr.*, vol. 7, pp. 045001, 2019.
6. M.J.G. Guimarey, J.L. Viesca, A. Abdelkader, B. Thomas, A. Hernández-Battez, M. Hadfield, “Electrochemically exfoliated graphene and molybdenum disulfide nanoplatelets as lubricant additives”, *J. Mol. Liq*., vol. 342, pp.116959, 2021.

Proceedings of the SICT/PlasmaTech/Tribology 2022 Joint International Conference
Barcelona, Spain – April 27 – 29, 2022
DOI: https://doi.org/10.26799/cp-sict-plasmatech-tribology-2022

Development of a Tribological Testing Method for Lubricating Oils in Weaving Machines.

Eleonora Colombo[1], Manuela Toscanini[2], Valerio Brocco[3]

[1] Downstream R&D Centre, Eni SpA
Via Felice Maritano 26, 20097 San Donato Milanese, Italy, eleonora.colombo@eni.com
[2] Downstream R&D Centre, Eni SpA
Via Felice Maritano 26, 20097 San Donato Milanese, Italy, manuela.toscanini@eni.com
[3] Downstream R&D Centre, Eni SpA
Via Felice Maritano 26, 20097 San Donato Milanese, Italy, valerio.brocco@eni.com

Abstract

Textile machines are used worldwide to produce woven fabrics; mechanical components move in fast relative motion and are continuously subjected to friction and wear. Proper lubricant design is fundamental to guarantee long-lasting operability and reduce energy consumption. In this work, a specific tribological test is developed to discriminate the lubrication ability of oils in weaving machines' gearboxes. The experimental activity is conducted in Eni laboratories using translatory oscillation tribometer SRV®5 with cylinder-on-disk configuration. Finely tuning of test parameters is investigated to simulate as much as possible real tribological contact in looms. Throughout the test, the friction coefficient is evaluated, while wear scar depth and cross-sectional area are measured at the end of the experiment. Different oils are tested, one commercial oil and 3 in-house formulated lubricants. The proposed procedure distinguishes oils able to build stable lubricating oil film between metallic surfaces from unstable ones by analysing friction coefficient trends.

Keywords: tribology, friction coefficient, wear, SRV®5, weaving machines, energy-saving lubricant.

1. Introduction

In the textile industry, different kinds of spinning, knitting, and weaving machines are employed; each of them needs proper lubrication. Mechanical sliding parts in weaving machines are subjected to oscillation, vibrations, high loads, and speeds; therefore, lubricating oils have to provide wear protection and scuffing load resistance [1]. In addition, good friction behaviour helps to reduce power losses and to improve energy efficiency [2]. The most relevant point where wear and friction need to be avoided is represented by the gearbox with a worm gear system [3]. Moreover, outstanding anti-oxidation properties are required to ensure oil-change intervals up to 20'000 hours and reduced maintenance costs. Synthetic oils are reported to perform well in these conditions; however, the additive package is relevant too. The scope of the developed experimental activity is to outline an ad hoc tribological test for linear sliding motion able to discriminate oils with promising lubrication properties against seizure and stick-slip from unsuitable lubricants in weaving looms.

2. Experimental apparatus

The tribological method is defined using SRV®5 apparatus developed by Optimol for the evaluation of friction and wear performances of lubricants and present in the Eni tribological laboratory. The SRV®5 system enables the oscillatory translational movement between two mechanical parts at different frequencies, loads, and strokes. For this experimental activity, the employed tribological coupling is the cylinder-on-disk as shown in Figure 1 because it is closer to real tribological contact in weaving machines. The upper test specimen is a cylinder of 6-mm diameter and 8-mm height, while the lower specimen is a disk with a diameter of 24 mm and a height of 7.9 mm [4]. The cylinder, made of steel AISI 52100 / 100Cr6, is forced to move in relative motion against the disk, which is made of the same special alloy as the loom's slider.

Mahr Perthometer PGK 120 profilometer allows the measurement of depth and cross-sectional area of wear scar on SRV disks after the end of the test.

DOI: https://doi.org/10.26799/cp-sict-plasmatech-tribology-2022

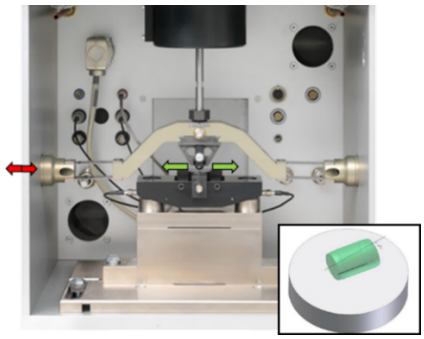

Fig. 1: SRV®5 tribometer and the cylinder-on-disk tribological coupling.

3. Tribological testing method

The testing procedure takes inspiration from antiwear screening tests for gear oils using SRV® tribometer [5]. However, tests parameters, i.e. load and temperature, need proper selection to replicate real operating conditions in weaving machines; tight collaboration with textile machine manufacturers is of pivotal importance. After a short running-in period, the normal force insisting on the upper cylinder is set to 80N to simulate contact pressures of textile gearboxes, and temperature is kept constant at 100°C. The test lasts 8 hours to highlight the stability trend of the oil film in time. The friction coefficient (COF) is recorded throughout the test duration each second [6]. Comparison with explorative tests of 3 hours confirms the test repeatability, friction coefficient mediated on 10 seconds may vary of ± 0.02.

Two reference lubricants are chosen: a commercial oil, commonly used in weaving machines, and the first formulated product (Lubricant 1), which led to the seizure of mechanical parts in the previous bench test. Additional in-house developed lubricants are formulated with low viscosity synthetic base oils, reported as Base 1 and Base 2, and specific additives.

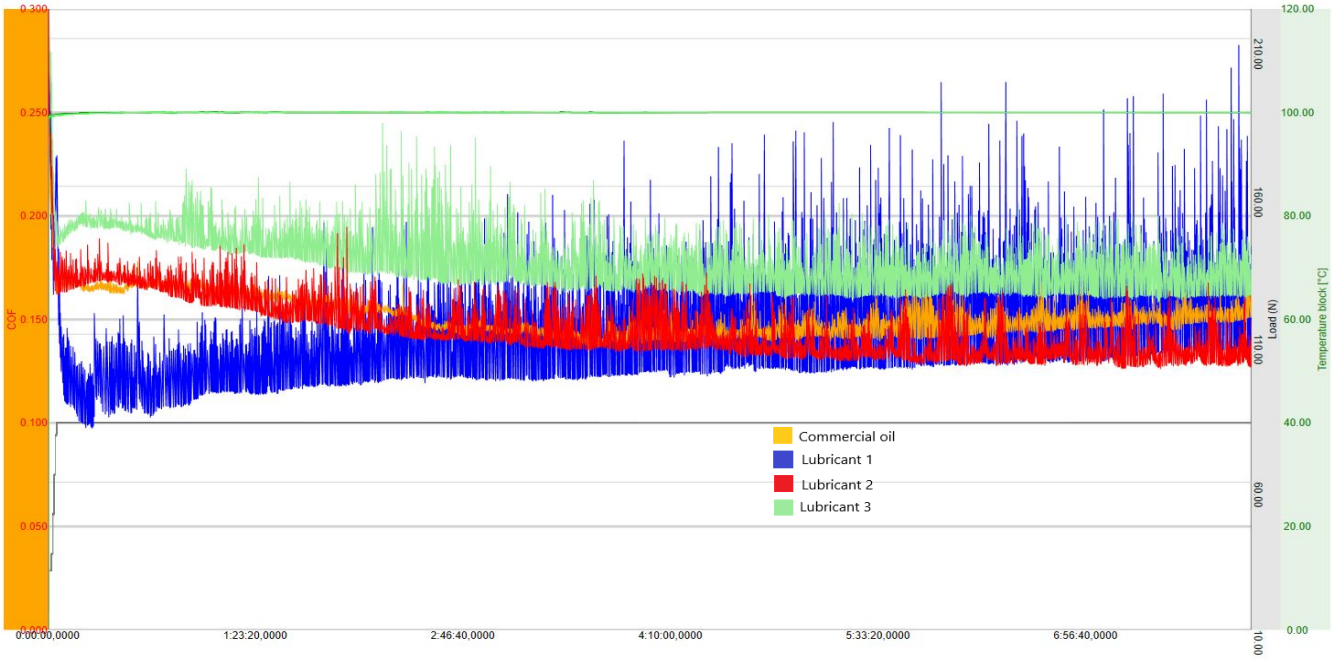

Fig. 2: Measured friction coefficient (COF) during the 8-hour test for commercial oil (yellow line), Lubricant 1 (blue line), Lubricant 2 (red line), and Lubricant 3 (green line).

4. Results and discussion

Initially, the above-presented test is performed on commercial lubricating oil and on Lubricant 1. Looking at Figure 2, it is possible to identify two completely different behaviours in terms of friction coefficient: the former

DOI: https://doi.org/10.26799/cp-sict-plasmatech-tribology-2022

lubricant is characterised by a progressively stabilizing trend with low spikes and mean friction coefficient reducing throughout the test, while the latter has an unstable behaviour with peaks of increasing intensity and with growing mean COF. The spikes represent micro-seizures due to inefficient lubrication and unstable oil film between the two metallic surfaces, pointing out the risk of mechanical failure. During sliding motion, the asperities of the two specimens come in contact, they generate localised welding and successive detachment because of continuous oscillatory movement [7][8]. The test is able to discriminate lubricants with successful properties from unsuccessful ones and properly guide lubricant design. A new formula is introduced by changing the additive package to enhance EP performance. Lubricant 2 is characterised by the same base oil as Lubricant 1, but its frictional behaviour is much more similar to commercial oil showing a stabilizing trend with small peaks. Moreover, as reported in Table 1, the depth and cross-sectional area of wear scar related to Lubricant 2 are limited, and the final mean friction coefficient is the smallest; this suggests that Lubricant 2 may be characterised by energy-saving performance. An additional formula is developed by introducing a different base oil; however, more peaks are detected with greater wear phenomena and higher mean friction coefficient. This is linked to the additive package, which works properly with different synthetic base oils.

Finally, it is worth noticing that results related to friction are expressed as peak-to-peak friction coefficient. When the cylindrical specimen reaches the two extreme positions of ± 1 mm with respect to the central position, COF is maximum because of static friction, as shown in Figure 3 by using the high-resolution analysis function of the SRV tribometer [9].

Table 1: Depth and cross-sectional area of wear scars on disks and final friction coefficients for all tested lubricants.

	Commercial oil	**Lubricant 1: Base 1 + Package A**	**Lubricant 2: Base 1 + Package B**	**Lubricant 3: Base 2 + Package B**
Depth [µm]	13.573	12.339	11.105	13.57
Area [µm^2]	11600	10000	8800	13300
COF	0.153	0.140	0.130	0.164

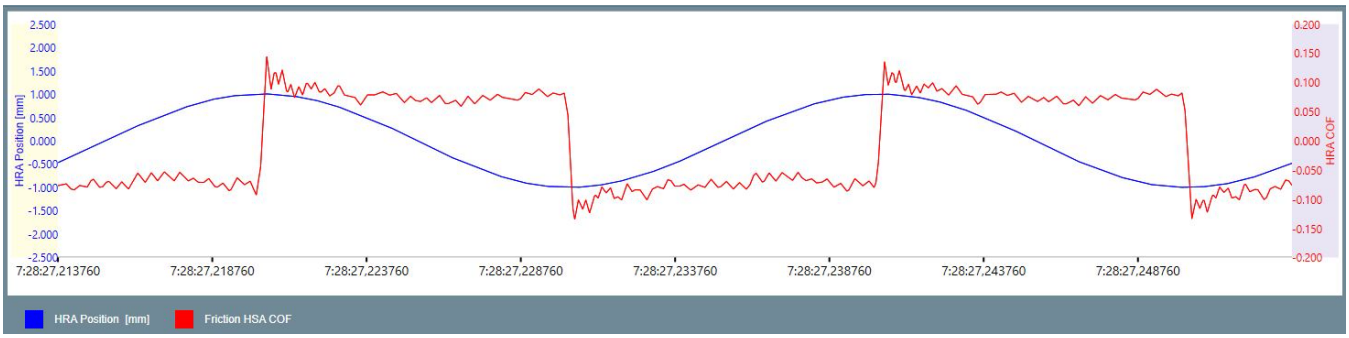

Fig. 3: HRA diagram for oscillation and friction coefficient close to the end of the test.

5. Additional oil requirements

Lubricating oils employed in textile machines need to meet additional physicochemical and tribological requirements. Anti-wear and EP properties have to be confirmed through 4-ball wear and 4-ball EP tests. Stick-slip tests are carried out to verify that the stick-slip ratio is lower than one. Besides, foaming tendency needs careful evaluation since foam must be avoided within the lubricating circuit. Washability, safety features, and anti-corrosion properties are checked too.

6. Conclusion

This experimental activity leads to the definition of an innovative in-house tribological test, which helps lubricant formulators in differentiating the lubricating ability of oils in weaving machines according to friction and wear results. The test is customized to follow the needs of the customers using peculiar materials provided by them and selecting suitable test parameters to replicate real machines' operating conditions. The proper

DOI: https://doi.org/10.26799/cp-sict-plasmatech-tribology-2022

combination between synthetic base oil and additive package may be identified and, as for commercial oil and Lubricant 2, it is characterized by a stable friction coefficient trend with decreasing mean value. Moreover, lower mean COF and limited wear highlight the possibility of reduced energy consumption by using Lubricant 2 in gearboxes. However, it is important to underline that tribological evidences have to be validated on selected field tests, which can be performed together with textile machines' manufacturers.

References

1. T. Mang, *Encyclopedia of Lubricants and Lubrication*. Springer, 2014.
2. J.Croes, A. Reveillere, S. Iqbal, D. Coemelck, B. Pluymers, W. Desmet, "A combined 1D-3D simulation approach for the energy analysis of a high speed weaving machine," in *Proceedings of ISMA2012-USD2012*, Leuven, 2012.
3. S. I. Ayon. (2021, August 11). "Maintenance of Weaving Machine in Textile Industry," [online]. Available: https://textilelearner.net/maintenance-of-weaving-machine/.
4. D. Massocchi, M. Lattuada, P. Pennacchi, S. Chatterton, "A tribological scale down from rig test to lab test: analysis on SRV experimental results as a screening for FZG rig test," in *MechE "29th Mission of Tribology Research"*, London, 2020.
5. C. Baumann, G. Patzer, "Using a translatory oscillation tribometer (SRV®) to screen gear oils," *STLE*, Minneapolis, MN, 2018.
6. Optimol Instruments, *SRV Operating Manual Machine*. Optimol Instruments Prüftechnik GmbH, Munich, version 34.
7. L. Deters, "Tribology," in *Springer Handbook of Mechanical Engineering*, Springer, Berlin, Heidelberg, 2009, pp.295-326.
8. "Gears - Wear and damage to gear teeth – Terminology," ISO 10825, 1995.
9. A. Schneider, "Rolling grease test adapter offers new testing opportunities," *Lube`n`greases EMEA*, vol. 12, issue 4, pp. 32-39, April 2018.

Proceedings of the SICT/PlasmaTech/Tribology 2022 Joint International Conference
Barcelona, Spain – April 27 – 29, 2022
DOI: https://doi.org/10.26799/cp-sict-plasmatech-tribology-2022

Tribological and Corrosion Properties of Coating Systems Dried by Infrared Radiation

Ivan Stojanović[1], Lovro Turkalj[1*], Ivan Cindrić[1], Ivan Juraga[1], Daniela Rakela Ristevski[2]

[1]Faculty of Mechanical Engineering and Naval Architecture, University of Zagreb
Ivana Lučića 5, Zagreb, Croatia, lovro.turkalj@fsb.hr
[2]Končar Steel Structures Inc.
Fallerovo šetalište 22, Zagreb, Croatia, daniela.rakela@koncar-mk.hr

Abstract

In many fields of industry, abrasion and erosion processes are dominant wear mechanisms that reduce lifetime of machine parts. Because of that, abrasion and erosion resistance must be taken into consideration due to coating wear over time which leads to premature corrosion and material breakdown. Coatings based on epoxy primers provide superior mechanical properties, such as hardness, durability, resistance to impacts, wear, and chemicals while maintaining exceptional adhesiveness, thus providing great protection in different corrosive environments. However, epoxy layers exposed to sun are prone to chalking due to the action of ultraviolet (UV) rays dissolving the binder. Because of that, polyurethane (PUR) topcoats are applied. Due to high abrasion, impact, and UV resistance, the defined EP/PUR coating system has proven to be an excellent corrosion and wear protection solution for top decks, exposed areas of car parks, exterior ship surfaces, helipads, balconies, and offshore platforms. Also, coatings must have a low environmental impact. More and more drastic environmental regulations aiming to reduce the emission of volatile organic compounds (VOC) in the atmosphere have led to developing water-based coatings which are increasingly used.

In this paper, water-borne and solvent-borne coating systems, with and without zinc in the primer, dried by infrared (IR) radiation and under atmospheric conditions were studied. To assess these differences, abrasion, erosion, hardness, and adhesion tests of the coating were performed. Anti-corrosion performance of the coatings was characterised using a salt spray chamber. Zinc rich (Zn (R)) coatings showed better tribological properties, with IR-dried coating systems displaying higher abrasion resistances. Solvent-borne coatings exhibited better corrosion properties than water-borne coatings when exposed to accelerated corrosion test in salt spray chamber. Both IR and air-dry coating curing technologies achieved adequate results with the difference of IR significantly reducing drying time.

Keywords: abrasion, erosion coating hardness, coating resistance, IR drying

1. Introduction

Main goal of any coating protection system is to protect tangible assets. Leading cause of degradation and damage to such assets is corrosion. In order to control corrosion, the coating system must be able to maintain all the stresses that occur during its use without premature deterioration [1]. Proper surface preparation and coating application contribute to its longevity, with constant requirements for impact loads and abrasion resistances during exploitation. Otherwise, coating may crack (with strong shocks) or wear out slowly (with constant flow of water or sand) exposing the substrate to water, salt, weathering, and finally, corrosion. Damage due abrasion or erosion manifests itself as damage that affects wider area around the place where loss of coating protection has occurred. In many industries such as marine, offshore, aerospace and mining, durability and safety must be ensured for parts such as valves, pumps, pipelines, turbine blades, etc. so that a given structure can withstand the demands of an erosive-corrosive environment [2,3]. Although the erosion process has been extensively studied, the mechanisms of polyurethane abrasive erosion remain unclear [4,5]. By applying IR drying technology, significantly higher drying speeds are achieved in addition to reduced gas consumption and combustion of volatile organic compounds. IR two-way drying method significantly accelerates chemical reactions in the coating which form the final coating ready for use at the time of drying [6]. “Dry sand / rubber wheel” and particle erosion tests were used to assess abrasion and erosion resistance properties.

DOI: https://doi.org/10.26799/cp-sict-plasmatech-tribology-2022

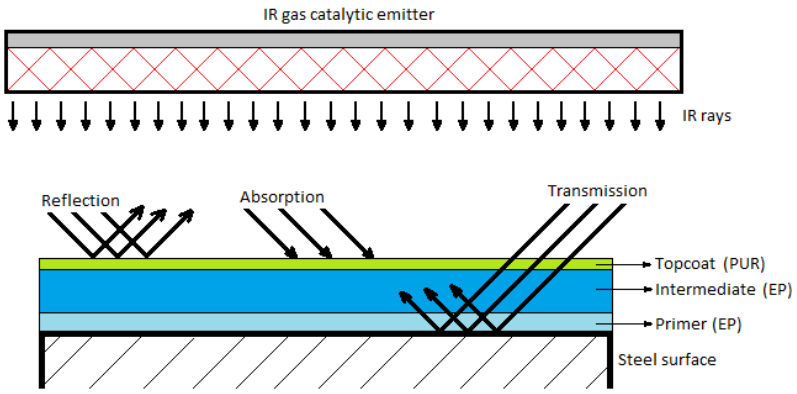

Figure 1. IR curing process of 3-layer coating system

2. Materials and methods

Solvent-borne (SB) and water-borne (WB) coating systems consisting of two component (2K) epoxy primer with and without zinc were tested. Half of the samples were dried by infrared (IR) radiation, while the other half was air-dried. Tested coatings were from two different paint manufacturers. Table 1. shows applied coating systems regarding the drying method, type of solvent and base coat. An IR chamber based on catalytic infrared radiation (CIR) was used to accelerate the drying process operating with wavelengths from 2 to 10 μm. Method used to test the abrasion resistance was dry sand / rubber wheel abrasion resistance test. Tests lasted from 3 to 5 seconds for each sample with loaded force of 45 N. Erosion wear and resistance test was performed by rotating the test specimens on the sample holder at high speed around the shaft with test times of 7, 14, and 21 minutes. Sample masses were measured before and after the test, therefore loss of mass was recalculated as the loss of volume ΔV. Accelerated corrosion test in salt spray chamber was performed to assess protective coating properties. Pencil and Pull-off tests were performed to evaluate coating hardness and adhesion properties.

Table 1. Applied coating systems with respect to drying method, type of solvent and base coat

Drying method	Sample	Applicated coating systems (primer-intermediate-topcoat)
IR/ atm.	A1/A2	SB: (Zn (R)) EP – EP - PUR
	B1/B2	SB: EP – EP - PUR
	C1/C2	WB: (Zn (R)) EP – EP - PUR
	D1/D2	WB: EP – EP - PUR
	E1/E2	SB: (Zn (R)) EP – EP - PUR
	F1/F2	SB: EP – EP - PUR
Abbreviations: SB (solvent-borne); WB (water-borne); (Zn (R)) – Zinc rich; EP – epoxy; PUR – polyurethane		

3. Results and discussion

Abrasion (Figure 1) and erosion (Figure 2) test results display that coating systems with Zn (R) primer generally having less volume loss than zinc free ones (A, C, E). WB coating system without zinc in primer (system D) had the highest loss of volume in abrasion and erosion wear tests compared to other coating systems. Air-dried sample had a higher loss of volume through abrasion and erosion tests in comparison with the coating system dried by IR. Coating systems containing zinc rich primers throughout erosion wear test have the same values as in abrasion wear tests, where system A has the highest resistance to erosion wear, followed up by system C and system E. For all three coating systems, IR drying has shown significantly better erosion wear resistances in comparison with air-cured ones. Observing from the manufacturer point of view, system A-D have shown better resistances to both abrasion and erosion wear tests than system E and F.

DOI: https://doi.org/10.26799/cp-sict-plasmatech-tribology-2022

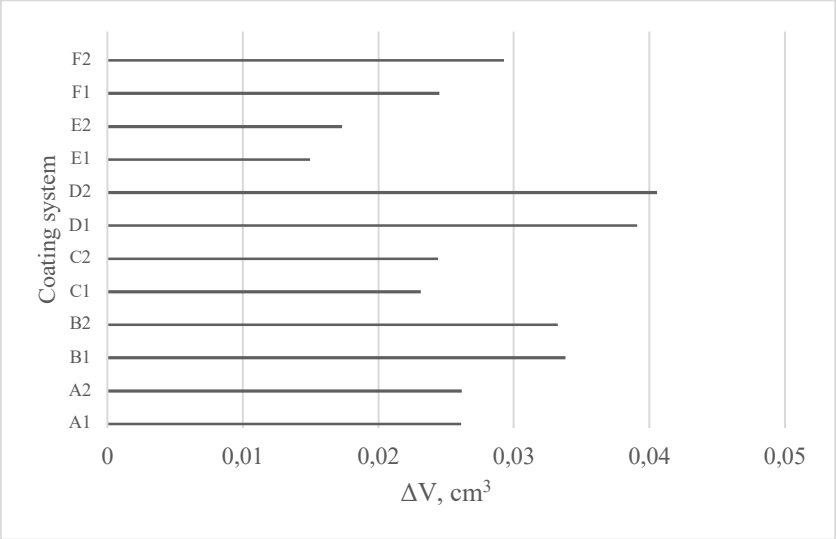

Figure 2. Average loss of coating volume during abrasion resistance test

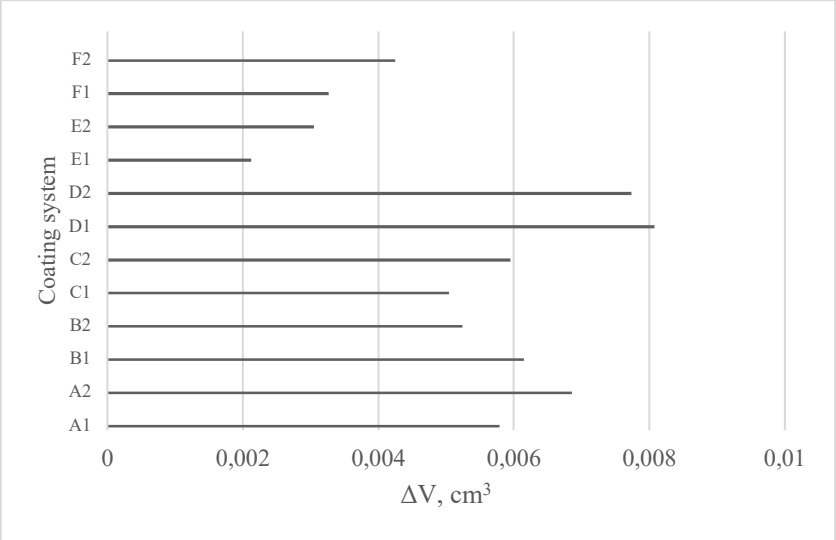

Figure 3. Average loss of coating volume during erosion resistance test

Physical tests were performed after 30 days (720 h) of accelerated corrosion test in salt spray chamber. Physical tests displayed that all coating systems fulfil the adhesion criterion with higher values than 12 MPa. The best adhesion properties achieved system E dried by IR radiation, while on air-cured systems highest adhesion value showed system B. Table 2. presents the results of physical test, in which can be seen systems D and C1 as the hardest, and system A2 as the softest one.

Table 2. Physical tests of coating systems after 720 h

Coating system	A1	B1	C1	D1	E1	F1	A2	B2	C2	D2	E2	F2
Pull-off [MPa]	17.06	18.18	17.98	12.9	19.97	15.61	13.7	15.43	12.42	13.4	15.2	14.68
Pencil test	HB	HB	H	H	HB	HB	B	HB	HB	H	HB	HB

4. Conclusion

Examined coating systems are primarily used in strong corrosive environment. Tribology examination tests display that Zn (R) primer systems have better abrasion and erosion resistances, with the advantage on IR drying

DOI: https://doi.org/10.26799/cp-sict-plasmatech-tribology-2022

technology. The cause may be the higher resistance of zinc particles to abrasion and erosion wear compared to pure epoxy. Following physical tests after exposing coating systems to salt spray chamber revealed a strong decline in adhesion and hardness properties for water-borne coating systems. Infrared curing technology has proven to be a reliable and quicker method of drying with no negative effect on the protective properties. However, coating systems which are used in aggressive abrasive and erosive environments should be reinforced with glass fibres or ceramic beads to increase tribological resistance.

Acknowledgements

This study is part of the project "Smart plant for drying liquid coatings" which is co-financed within the Operational Programme Competitiveness and Cohesion from the European Regional Development Fund under reference number KK.01.2.1.02.0030. The content of the published materials is the sole responsibility of the Faculty of Mechanical Engineering and Naval Architecture.

References

1. Tator K., Coating detoriation, 2015, ASM Handbook, Protective Organic Coatings. Volume 5B
2. Alqallaf J., Ali N., Amaral Teixeira J., Addali A. (2020). Solid Particle Erosion Behaviour and Protective Coatings for Gas Turbine Compressor Blades-A Review. Processes 8, 984.
3. Wood R.J.K. The sand erosion performance of coating. Materials and Design 20, pp. 179 – 191, Elsevier.
4. Malaki M., Hashemzadeh Y., Fadaei Tehrania A. (2018). Abrasion resistance of acrylic polyurethane coatings reinforced by nanosilica. Progress in Organic Coatings 125, pp. 507–515, Elsevier.
5. Zhang S.W., Renyang He, Deguo W., Qiyun F. (2001). Abrasive erosion of polyurethane. Journal of Materials Science 36, pp. 5037 – 5043, Kluwer Academic Publishers.
6. Stojanović, I. Cindrić, I. Janković, L. Šimunović, V. Franjić, H. (2022). Performance Assessment of Differently Dried Coating Systems for Potential Application in the Power Transformer Industry. Coatings 2022, 12, 331. https://doi.org/10.3390/coatings12030331

Proceedings of the SICT/PlasmaTech/Tribology 2022 Joint International Conference
Barcelona, Spain – April 27 – 29, 2022
DOI: https://doi.org/10.26799/cp-sict-plasmatech-tribology-2022

Triboscopic Investigation of Self-Mated Carbon Coatings in Non-Lubricated Friction Conditions

Lars Lorenz[1,2], Fabian Härtwig[1,2], Stefan Makowski[2], Matthias Krause[3], Andrés Fabián Lasagni[1,2]

[1]Institute of Manufacturing Science and Engineering, Technische Universität Dresden
George-Bähr-Strasse 3c, 01069 Dresden, Germany, lars.lorenz@tu-dresden.de (L.L.); fabian.haertwig@tu-dresden.de (F.H.), andres_fabian.lasagni@tu-dresden.de (A.F.L.)
[2]Fraunhofer Institute for Material and Beam Technology IWS
Winterbergstrasse 28, 01277 Dresden, Germany, stefan.makowski@iws.fraunhofer.de (S.M.)
[3]Institute of Ion Beam Physics and Materials Research, Helmholtz-Zentrum Dresden-Rossendorf, Bautzner Landstrasse 400, 01328 Dresden, Germany, matthias.krause@hzdr.de (M.K.)

Abstract

Tetrahedral amorphous carbon (ta-C) has shown to exhibit exceptionally low friction and wear under dry sliding in the presence of water vapor as well as acceptable low friction and wear in the presence of inert gases. However, it is known that these properties deteriorate rapidly under vacuum conditions with decreasing pressure.

For a better understanding of the wear mechanisms in doped and undoped ta-C coatings under vacuum and dry conditions, more advanced triboscopic imaging methods in regard to these systems were developed. Triboscopy is the imaging of the evolution of a tribosystem via combination of highly-resolved local and spatial information, most often the evolution of friction.

The experimental data of self-mated ta-C contacts in air and vacuum shown in this study was obtained from a custom-built ultra high vacuum tribometer in ball-on-disc configuration. Based on these experiments, the resulting triboscopic images are discussed based on their triboscopic features according to the persistence in both track position and time. The resulting specific triboscopic features are correlated to distinct wear phenomena, demonstrating the increased analytical capabilities when compared to conventional friction curves and wear track images. While in the context of this work the correlations were made after the experiments, the use of these findings for monitoring in-line experiments can strongly enhance the capability of monitoring tribological systems in the future.

Keywords: ta-C, a-C, DLC, wear, triboscopy

1. Introduction

Friction analyses of tribological experiments are commonly reduced to friction curves, which represent the coefficient of friction, e.g., by averaging friction coefficients during a certain number of cycles or by picking specific points in a cycle. Wear analyses are usually performed ex-situ after the tribological test, and the temporal evolution of wear must be reconstructed by correlation with the friction curves. A separate examination of different parts of the wear track regarding temporal progression is therefore not possible. To overcome this obstacle, in-situ methods with e.g., microscopes, Raman spectrometers, and FTIR spectrometers have been applied, but are either expensive or limited to certain counter body materials [1-3]. In addition, these are often not feasible for vacuum tribometer setups.

These analytical shortcomings can be overcome for most tribological tests using triboscopy. Triboscopy is the coupling of tribological information with the numerical process of the recorded information creating an image [4,5]. This idea usually manifests in the two-dimensional visualization of, e.g., friction for both position and time during or after a tribological experiment. This also allows attributing changes to specific positions in the wear track [6].

Hydrogen-free tetrahedral amorphous carbon (ta-C) is a form of carbon (also sometimes called diamond-like carbon (DLC)) with a high degree of sp^3-hybridized atoms (exceeding 50 at%). Furthermore, the degree of sp^3-hybridized atoms determines mechanical properties of the material, including density, hardness, and Young's modulus, making ta-C the hardest type of amorphous carbon [7,8]. In addition to its outstanding mechanical properties, ta-C coatings also show a beneficial tribological behavior (low friction and wear) that enables its

DOI: https://doi.org/10.26799/cp-sict-plasmatech-tribology-2022

application as friction-reducing and/or wear protection coatings on highly stressed, oil-lubricate components, e.g., on automotive engine components [9-11]. On the other hand, under dry friction conditions, ta-C exhibits widely different friction and wear behavior depending mostly on the presence of water vapor [12].

The use of triboscopy for localized friction analysis has been suggested by dos Santos et al., along with showing several relevant applications [13] and an application in the field of carbon films was demonstrated by Fontaine et al. in their research on the healing effect of hydrogen gas on a-C:H films [14].

In this study, we apply the concept of triboscopy to dry friction experiments done on self-mated hydrogen-free carbon coatings. The main objective is to demonstrate the methodology of triboscopy on these tribological measurements for the correlation of triboscopic features with wear phenomena.

2. Materials and Methods

A ta-C coating was deposited using the Laser-Arc technique [15] with a commercial PVD coating system. The coating was produced from a pure graphite cathode. Steel disks made of hardened low-alloy chromium steel (100Cr6, EN 1.3505) with a diameter of 24 mm and a thickness of 6.9 mm were used as substrates for the different coatings.

After deposition, different characteristics of the coating systems were determined on steel reference samples. The coating thicknesses were measured by ball crater method. Mechanical properties were derived from nanoindentation experiments, using a ZwickRoell ZHN nanomechanical test system (Ulm, Germany) according to [16]. Prior to tribological testing, the deposited coatings were polished with diamond suspension to a roughness of $Ra < 20$ nm. For the tribological tests, counter bodies made from steel were also coated with ta-C.

The tribological measurements in this work were carried out using an ultra-high vacuum tribometer (Tetra Basalt UHVT-14, Ilmenau, Germany) in rotating configuration. The measurements were performed using a normal load of 5 N, a velocity of 3 $mm \cdot s^{-1}$ with a sliding distance of 12 m. The data was sampled at 1 kHz rate. All the experiments were performed in dry conditions without adding lubricants. Three different atmospheres were employed: humid air (90% RH) and vacuum (10 mbar and 10^{-2} mbar) under ambient temperatures.

From the recorded raw data, triboscopic images have been prepared. Since a rotational setup was used, the position of the ball on the sample was defined as angular position. In the following, triboscopic images of friction coefficient data will be discussed. The classification of triboscopic features is described in more detail in [17] and distinguishes between GLOBAL, LOCAL, UNIFORM and SPORADIC. For the GLOBAL case, the triboscopic value changes over time, but does so for all positions in the track equally. This hints at a structural change on the moving counter body, e.g., the formation of a tribolayer. For the LOCAL case, there are persistent features at certain positions, which hint changes on the lower sample side. For the UNIFORM case, no significant change can be observed during the experiment. Lastly, the SPORADIC case specifies features that neither persist in the position nor the cycle.

3. Results and Discussion

The results of the tribotesting of the ta-C/ta-C pairing in different atmospheres is shown in **Figure 1**. As expected, the experiment in humid air (**Figure 1a**) has generally UNIFORM behavior. The coefficient of friction decreases slightly from 0.08 to 0.06 over the course of the experiment, which is caused by the gradual, slight smoothing of both coatings. The triboscopic imaged derived from the experiment in a 10 mbar vacuum is shown in **Figure 1b**. For the first 50 cycles a GLOBALLY high coefficient of friction can be observed. Afterwards, the coefficient of friction drops to levels comparable to the humid case. This is explained by the initially high contact pressure, which decreases due to the steadily increasing contact area due to wear, eventually stabilizing as soon as the ball coating wear is low enough that remaining water in the vacuum is sufficient to passivate the surface. Of further interest are the sporadic features in the low-friction area, which manifest as diagonal lines in the direction of movement [17]. These can be attributed to wear particles, which are carried a short distance in the contact and picked up in the next cycle. These particles are likely to occur from brittle failure of the coating and detachment of embedded growth defects, leading to loose and hard particles in the contact area. In conventional analysis of the friction curve, shown beneath the triboscopic image, such behavior is usually not visible. In a 10^{-2} mbar vacuum (**Figure 1c**), these same SPORADIC features can also be observed, which again

DOI: https://doi.org/10.26799/cp-sict-plasmatech-tribology-2022

indicates the continuous generation of wear particles, which get dragged along in the wear track over several cycles. The friction coefficient outside of the SPORADIC features does not recover from the initially high value, due to an insufficient amount of trace water vapor to achieve surface passivation. This reveals that for this pairing friction is mostly governed by surface passivation, independent from generated wear debris.

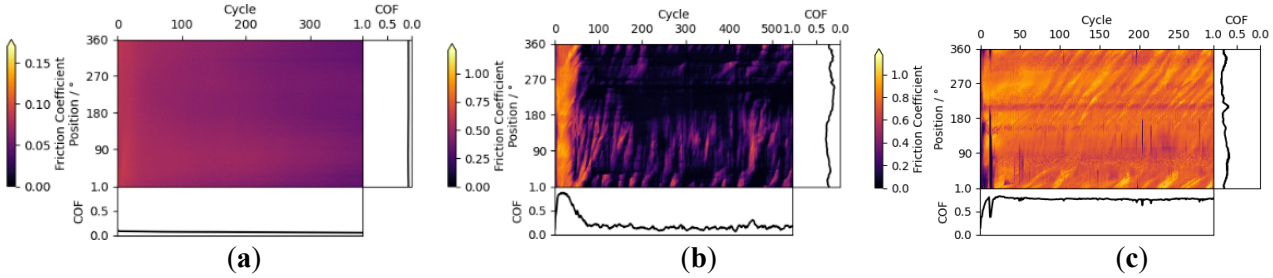

Figure 1. Friction triboscopic images of a ta-C coatings vs. a ta-C-coated ball in various atmospheres; (**a**) in humid air, showing UNIFORM triboscopic features (**b**) in a 10mbar vacuum, showing a global change in the friction coefficient at cycle #50 and distinct sporadic features from wear debris for the remaining measurement; (**c**) in a 10^{-2} mbar vacuum, showing consistently high friction and additionally sporadic features due to wear debris. Modified from [17]

4. Conclusion

In this work, the triboscopy method was applied to friction experiments of a self-mated ta-C contact in humid air and vacuum. The resulting triboscopic features were correlated with wear and friction processes, namely surface passivation and wear debris generation. It could be shown that no significant tribological changes occur under humid conditions and while in a 10 mbar vacuum wear debris starts to be generated. On the other hand, this characteristic does not automatically lead to a significant overall increase in friction. Differently, it was found that at 10^{-2} mbar vacuum, a different behavior occurs, where the lack of environmental water leads to high friction from the lack of surface passivation.

Based on these experiments it could be demonstrated that triboscopy allows for friction and wear processes to be studied in more detail, enabling direct correlation of tribological and triboscopy features in both location and time, far exceeding the possibilities from conventional friction curves. Many tribometers can provide high-rate data for friction and position, real-time triboscopic evaluation of such data can give detailed in-situ access to tribological processes without adding any costly instrumentation.

Acknowledgements

This work was supported by the Deutsche Forschungsgemeinschaft (DFG – German Research Foundation) under grant agreement 415726702.

References

1. Okubo, H.; Sasaki, S.; Lancon, D.; Jarnias, F.; Thiébaut, B. Tribo-Raman-SLIM Observation for Diamond-like Carbon Lubricated with Fully Formulated Oils with Different Wear Levels at DLC/Steel Contacts. *Wear*, **2020**, *454–455*, 203326. https://doi.org/10.1016/j.wear.2020.203326
2. Singer, I. L.; Dvorak, S. D.; Wahl, K. J.; Scharf, T. W. Role of Third Bodies in Friction and Wear of Protective Coatings. Journal of Vacuum Science & Technology A: Vacuum, *Surfaces, and Films*, **2003**, *21*, S232–S240. https://doi.org/10.1116/1.1599869
3. Mangolini, F.; Rossi, A.; Spencer, N. D. In Situ Attenuated Total Reflection (ATR/FT-IR) Tribometry: A Powerful Tool for Investigating Tribochemistry at the Lubricant–Substrate Interface. *Tribology Letters*, **2011**, *45*, 207–218. https://doi.org/10.1007/s11249-011-9868-5
4. Belin, M. Triboscopy: A New Quantitative Tool for Microtribology. *Wear*, **1993**, *168*, 7–12. https://doi.org/10.1016/0043-1648(93)90190-w
5. Belin, M.; Martin, J. M. Triboscopy, a New Approach to Surface Degradations of Thin Films. *Wear*, **1992**, *156*, 151–160. https://doi.org/10.1016/0043-1648(92)90150-7
6. Sánchez-López, J. C.; Belin, M.; Donnet, C.; Quirós, C.; Elizalde, E. Friction Mechanisms of Amorphous Carbon Nitride Films under Variable Environments: A Triboscopic Study. *Surface and Coatings Technology*, **2002**, *160*, 138–144. https://doi.org/10.1016/s0257-8972(02)00397-3

7. Robertson, J. Diamond-like Amorphous Carbon. *Materials Science and Engineering: R: Reports*, **2002**, *37*, 129–281. https://doi.org/10.1016/s0927-796x(02)00005-0
8. Ferrari, A. C. Diamond-like Carbon for Magnetic Storage Disks. *Surface and Coatings Technology*, **2004**, *180–181*, 190–206. https://doi.org/10.1016/j.surfcoat.2003.10.146
9. Erdemir, A.; Donnet, C. Tribology of Diamond-like Carbon Films: Recent Progress and Future Prospects. *Journal of Physics D: Applied Physics*, **2006**, *39*, R311–R327. https://doi.org/10.1088/0022-3727/39/18/r01
10. Kennedy, M.; Hoppe, S.; Esser, J. Lower Friction Losses With New Piston Ring Coating. MTZ worldwide, **2014**, *75*, 24–29. https://doi.org/10.1007/s38313-014-0135-7
11. Kano, M. Overview of DLC-Coated Engine Components. Coating Technology for Vehicle Applications, **2015**, 37–62. https://doi.org/10.1007/978-3-319-14771-0_3
12. Andersson, J.; Erck, R. A.; Erdemir, A. Friction of Diamond-like Carbon Films in Different Atmospheres. *Wear*, **2003**, *254*, 1070–1075. https://doi.org/10.1016/s0043-1648(03)00336-3
13. dos Santos, M. B.; Costa, H. L.; De Mello, J. D. B. Potentiality of Triboscopy to Monitor Friction and Wear. *Wear*, **2015**, *332–333*, 1134–1144. https://doi.org/10.1016/j.wear.2014.10.017
14. Fontaine, J.; Belin, M.; Le Mogne, T.; Grill, A. How to Restore Superlow Friction of DLC: The Healing Effect of Hydrogen Gas. *Tribology International*, **2004**, *37*, 869–877. https://doi.org/10.1016/j.triboint.2004.07.002
15. Kaulfuss, F.; Weihnacht, V.; Zawischa, M.; Lorenz, L.; Makowski, S.; Hofmann, F.; Leson, A. Effect of Energy and Temperature on Tetrahedral Amorphous Carbon Coatings Deposited by Filtered Laser-Arc. *Materials*, **2021**, *14*, 2176. https://doi.org/10.3390/ma14092176
16. Lorenz, L.; Chudoba, T.; Makowski, S.; Zawischa, M.; Schaller, F.; Weihnacht, V. Indentation Modulus Extrapolation and Thickness Estimation of Ta-C Coatings from Nanoindentation. *Journal of Materials Science*, **2021**, *56*, 18740–18748. https://doi.org/10.1007/s10853-021-06448-2
17. Lorenz, L.; Makowski, S.; Weihnacht, V.; Krause M.; Lasagni, A. F. Advantages of Using Triboscopic Imaging: Case Studies on Carbon Coatings in Non-Lubricated Friction Conditions. [Manuscript submitted for publication]

Proceedings of the SICT/PlasmaTech/Tribology 2022 Joint International Conference
Barcelona, Spain – April 27 – 29, 2022
DOI: https://doi.org/10.26799/cp-sict-plasmatech-tribology-2022

Biobased functional coatings for cellulosic substrates

Maria-Beatrice Coltelli [1,2], Luca Panariello[1,2,] Vito Gigante[1,2], Laura Aliotta[1,2], Simone Giangrandi[3], Ahdi Harich[5], Ilaria Canesi[5], Andrea Lazzeri[1,2,5], Patrizia Cinelli[1,2]

[1] National Interuniversity Consortium of Materials Science and Technology (INSTM), Via Giusti 9, 50121, Firenze, Italy, patrizia.cinelli@unipi.it
[2]Department of Civil and Industrial Engineering, University of Pisa, Via Diotisalvi 2, 56122, Pisa, Italy, maria.beatrice.coltelli@unipi.it
[3]LUCENSE SCaRL, Traversa prima di Via della Chiesa di Sorbano del Giudice 231, 55100 Lucca, Italy, simone.giangrandi@lucense.it
[4] Biomass Valorization Platform-Materials, CELABOR s.c.r.l., 4650 Chaineux, Belgium, ahdi.hadrich@celabor.be
[5]Planet Bioplastics s.r.l., Via Diotisalvi, 2, 56122 Pisa, Italy, andrea.lazzeri@unipi.it

Abstract

Biobased and biodegradable anti-microbial coatings for cellulosic board are valuable for preparing a packaging that can preserve for long time the contained products, granting safeness to the packaged product and an optimized end of life. Chitin nanofibrils and chitosan can be obtained by chitin, widely diffused in arthropods waste (shrimps, crabs or insects) or in mushrooms. Chitin nanofibrils or chitosan have been used for the preparation of liquid water-based coatings for paperboard used for packaging. The application of liquid coatings based on chitosan and chitin nanofibrils to cellulosic board was carried out by using a cylindrical steel bar and an automatic applicator equipped with a universal blade. A virgin and a recycled board were used for comparison. The used chitin nanofibrils are obtained by an innovative and environmentally friendly methodology based on a mild deacetylation step followed by a mechanical treatment. The anti-microbial and mechanical properties of the coated cellulosic board are thus compared. Interestingly the application of chitosan and chitin nanofibrils resulted in different mechanical properties for the treated virgin and recycled paperboard, but both coatings showed anti-bacterial properties, much evident for recycled board. Hence, these chitin derivatives can be used not only for producing fully biobased anti-microbial coating for packaging, but also for supporting the use of recycled cellulosic fibers in several products.

Keywords: biobased coatings; Functional coatings; chitin; chitosan; nanofibrils;

1. Introduction

Cellulosic substrates, as renewable and recyclable items, are highly used in the packaging and personal care field. Recycled cellulosic fibers of high quality are also available from several recycling plants and they should be used more extensively to grant a wider application of circular economy principles [1]. However, to expand the use of virgin and recycled cellulosic substrates in several applications and improve their properties, the application of a functional coating improving the barrier to oxygen, water vapour of the substrate or anti-microbial properties is fundamental, especially in packaging applications. This coating should be biobased and not affecting the end-of life of the final packaging or personal care product (recycling and/or composting). Several coatings were proposed based on biopolymers like proteins, chitin or cutin [2], [3].

Chitin is a very abundant polymer available from crustaceans exoskeletons (sea food waste)[4], from insects[5] or from mushrooms [6]. It can be converted to chitin nanofibrils or chitosan on the basis of the adopted process. Interestingly chitin nanofibrils were found cytocompatible, show anti-inflammatory activity and may serve for the delivery of biomolecules for skin care and cells regeneration [7], [8]. Chitin nanofibrils (CN) and chitosan-based coatings can confer to cellulosic board anti-microbial properties, so they can be considered as functional coatings for increasing the shelf life of packaging for fresh food [9]. Chitin nanofibrils can be produced with a chemical methodology based on the use of acids [10] that should be improved to decrease its environmental impact. Mechanical treatments could be considered alternative, nevertheless, due to the strong hydrogen bonds between chitin nanofibers, large amounts of energy are needed to disintegrate chitin fibrils into nanofibers via mechanical treatments. High-pressure homogenization [11] and disk milling can circumvent the problem of high energy consumption during mechanical processes, chemical pre-treatment by TEMPO (2,2,6,6-tetramethylpiperidine-1-oxyl radical)-mediated oxidation was used to weaken the bonds that hold the chitin

DOI: https://doi.org/10.26799/cp-sict-plasmatech-tribology-2022

chains together making it easier to break them into CN[12]. Partial deacetylation associated with partial mechanical scission of the fibrils during disintegration was also used to obtain CN and this seems the best compromise[13] to efficiently obtain a nano-structured material with a limited use of strongly acidic chemicals.

In the present paper we report the results related to the application of liquid coatings based on chitosan and chitin nanofibrils to cellulosic board. In the attempt of widening the impact of our research, a virgin and a recycled board are used for comparison. The used chitin nanofibrils are obtained by a new methodology based on a deacetylation step followed by a mechanical treatment. The anti-microbial and mechanical properties of the coated cellulosic board samples are compared with the aim of selecting biobased functional coatings suitable for specific packaging applications.

2. Materials and method

2.1. Materials

Cellulosic virgin and recycled boards having a thickness of 400 µm were provided by LUCENSE. Chitosan powder, low viscosity grade, was bought from Sigma Aldrich (Missouri, USA).

Partially deacetylated chitin nanofibrils (CN) suspension (Aldrich, Shrimp-based, water solution 1.7 wt%) was supplied by Celabor (Chaineux, Belgium). The suspension was obtained through a chemical pre-treatment followed by a mechanical defibrillation process using an ultra-fine friction grinder Super masscolloider (Masuko® Sangyo co. ltd, Japan) equipped with two ceramic nonporous grinders adjustable at any clearance between the upper and lower grinder. Chemical pre-treatment was performed by a partial deacetylation of commercial chitin from shrimp shells (Sigma-Aldrich, Belgium) using concentrated sodium hydroxide. The reaction was stopped when a degree of deacetylation (DDA) of 16% was reached. The product was then purified until the pH value reached 6.5~7. After the partial deacetylation, the resultant chitin suspensions were then prepared for mechanical defibrillation by dispersing them in acidified water at a concentration of 1.7 wt%. The solution was then manually poured into the grinder and the partially deacetylated chitin suspensions fed into the hopper were dispersed by centrifugal force into the clearance between the grinding stones, where they were ground into ultra-fine particles, after being subjected to massive compression, shearing and rolling friction forces. CN were thus obtained as a stable gel and stored at 4 °C until further use.

2.2. Methods

Celabor chitin gel was directly applied on the substrates and a wet coating of 220 µm was applied on virgin and recycled board. Sigma Aldrich low viscosity chitosan was dissolved into an acetic acid (AcOH) solution at 1% w/w for a final chitosan concentration of 2,5% w/w in the solution and then a wet coating of 150 µm was applied onto the cellulosic substrates.

An automatic applicator Zehntner ZAA 2300 (Sissach, Switzerland) equipped with a universal applicator Zehntner Zua 2000 (Sissach, Switzerland) was used to perform a homogeneous coating onto the substrates. The application speed was 10 mm/sec, the width of applicator was 20 cm and the thickness was calculated for every sample. Coatings were applied under a fume hood at room temperature to promote the evaporation of the solvent (acidic water).

The morphology of CN was observed with a scanning electron microscopy using a FEI Quanta 450 ESEM FEG scanning electron microscope.

The evaluation of the stiffness of the board after treating was carried out with a bending-stiffness tests. Tests were conducted using two-point bending method with a 50mm bending length and a 15° bending angle by a Lorentzen & Wettre apparatus. Moreover, the thickness of dry treated board was determined.

Antibacterial properties of chitin suspensions were tested on treated cardbord according to BS ISO 8784-2:2014 Standard for determining the total number of colony-forming units of bacteria on suface.

3. Results and discussion

CN was characterized by electron microscopy and it was possible to observe its nano-structural morphology, characterized by the presence of nano-fibrils (Figure 1a).

DOI: https://doi.org/10.26799/cp-sict-plasmatech-tribology-2022

From a previous work[9] it was observed that the application of a layer of 150 µm of chitin-chitosan dispersion (2,5% w/w) provided an antimicrobial effect on cellulosic board substrates. Hence, considering the thickness of the present boards, the correct amount of treatment was applied on each substrate considering the lower concentration of CN and following a linear proportion. Thus, CN gel was directly applied on the substrates. In particular, wet coating of 220 µm was applied on virgin (figure 1b and c) and recycled board.

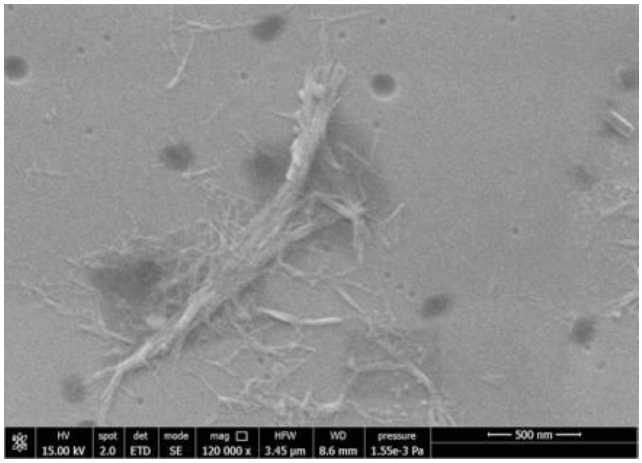

(a)

(b)

(c)

Fig. 1: (a) SEM micrograph showing nanostructured chitin nanofibrils present in the coating; (b) virgin board; (c) CN coated virgin board;

Bacteria contact plate tests were adopted for testing the anti-microbial properties of samples, following the ISO/DIS 8784-2 standard for pulp, paper and board, for the enumeration of bacteria, yeast and mould on surface. The results are reported in table 1.

Table 1: Results of antimicrobial tests

Sample	TOTAL BACTERIA – CONTACT PLATE			MOLDS/YEASTS – CONTACT PLATE		
	Colonies	Area (cm²)	UFC/100 cm²	Colonies	Area (cm²)	UFC/100 cm²
Virgin pure	3	72	4	1	72	1
Recycled pure	835	72	1.160	4	72	6
Virgin + CN	5	72	7	19	72	26
Recycled + CN	13	72	18	17	72	24
Virgin + Chitosan	0	72	0	5	72	7
Recycled + Chitosan	28	72	39	30	72	42

By analysing the results it can be noticed the antibacterial effect of both chitin and chitosan on recycled board packaging. The results showed also that CN is slightly more effective as antibacterial additive than chitosan. It was not possible to evaluate the antimicrobial properties of the treatments on the virgin board because all the

DOI: https://doi.org/10.26799/cp-sict-plasmatech-tribology-2022

test, including the not treated sample, gave a zero growth of bacteria. No effect was evidenced of both chitosan and CN against molds and yeasts.

The thickness of treated and not treated boards were determined after drying them and conditioning at 23°C/50%r.h. (according to ISO 534 2011). The thickness of the dry coating was thus determined. The chitosan coating resulted less thick than the CN coating. In particular, results indicated that the chitin form a layer of about 50 microns while the chitosan form a layer of about 20 microns.

Table 2: Results of Results of thickness and stiffness evaluation

Sample	Treated board Thickness (µm)	Dry treatment thickness (µm)	Treated board Stiffness (mN)	Dry treatment Stiffness (mN)
Virgin pure	478	-	352	-
Recycled pure	390	-	152	-
Virgin + CN	539	61	429	77
Recycled + CN	438	48	194	42
Virgin + Chitosan	496	18	368	15
Recycled + Chitosan	412	22	181	29

Considering that the weight percentage of chitin or chitosan in each treatment was the same, the difference of thickness may be attributed to a different moisture content or to the nanostructured feature of the chitin treatments. From a mechanical point of view, the stiffness is strictly correlated to the thickness. In fact, chitosan, having more evident filming properties because soluble in the water-based treatment, forms a more compact layer than chitin. The chitosan soluble coating is partially penetrated in board porosity, thus its effect on thickness increase is reduced. The chitin nanofibrils based coating has also, filming capacity. Nevertheless, chitin nanofibrils are not soluble, but nanosuspended in the gel-like coating. Thus, the coating consists of nanofibrils interacting one another and with cellulose microfibers with strong hydrogen bonding. Nanofibrils can deposit well on the cellulosic network, remaining on the surface and affecting more the intrinsic mechanical properties of the board because of their fibrous interconnected and thus reinforced structure. This can represent an advantage with respect to chitosan in cellulosic substrates, as a reinforcing effect can be exploited by using CN. Reasonably, both coating has a strong adhesion and compatibility with cellulose, because of their common polysaccharidic nature.

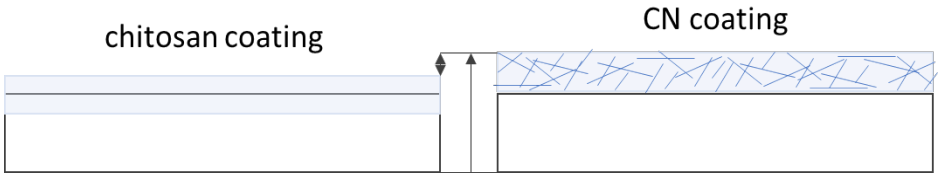

Fig. 2: light blue coating on the white cellulosic network of board: on the left chitosan solution, partially penetrating in board porosity; on the right CN based coating, depositing on the surface where an interconnected nano-net is formed.

Moreover, thanks to this deposition of nanofibrils on cellulose surface the anti-microbial properties are confined on the surface region of the sample. On the other hand, in the case of soluble chitosan solution, much chitosan penetrates inside the cellulosic material, so it is not available on the coated substrate. Moreover, a nanofibrous surface area (like the one of CN treatment) is wider than the surface area of a cast film (like the one of chitosan coating). Reasonably this different behaviour explains the better anti-microbial properties of CN than chitosan.

4. Conclusion

A chitosan and a chitin nanofibrils (CN) water-based coatings were successfully applied on virgin and recycled paperboard by using and automatic film applicator. The coatings showed a high homogeneity and the recycled board treated with CN and chitosan resulted anti-bacterial. CN treated board showed slightly better anti-bacterial properties than chitosan treated board. Moreover, the CN coating showed a better reinforcing effect on mechanical properties than chitosan one. The differences were attributed at the soluble and insoluble nature

DOI: https://doi.org/10.26799/cp-sict-plasmatech-tribology-2022

of chitosan and CN, respectively, inducing also a better confinement on board surface of CN than chitosan. Thanks to the performed work new biobased functional coating for cellulosic substrates were developed. Thus, this work facilitated a more extended use of cellulosic substrates in packaging. In particular, an extended use of recycled cellulosic fibers can be predicted thanks to the use of such coatings.

Acknowledgements

This research was funded by the Bio-Based Industries Joint Undertaking under the European Union Horizon 2020 research program (BBI-H2020), ECOFUNCO project, grant number G.A 837863; We thank the Centre for Instrumentation Sharing-University of Pisa (CISUP) for their support in the use of FEI

Quanta 450 FEG scanning electron microscope.

References

1. S. Escursell, P. Llorach-Massana and M. B. Roncero, “Sustainability in e-commerce packaging: A review,” *J. Clean. Prod.*, vol. 280, p. 124314, 2021, doi: 10.1016/j.jclepro.2020.124314.
2. V. Gigante, L. Panariello, M.B. Coltelli, S. Danti, K.A. Obisesan, A. Hadrich, A. Staebler, S. Chierici, I. Canesi, A. Lazzeri, P. Cinelli, “Liquid and solid functional bio-based coatings,” *Polymers (Basel).*, vol. 13, no. 21, pp. 1–22, 2021, doi: 10.3390/polym13213640.
3. M.B. Coltelli, F. Wild, E. Bugnicourt, P. Cinelli, M. Lindner, M. Schmid, V. Weckel, K. Müller, P. Rodriguez, A Staebler, L. Rodríguez-Turienzo and A. Lazzeri, “State of the Art in the Development and Properties of Protein-Based Films and Coatings and Their Applicability to Cellulose Based Products : An Extensive Review,” pp. 1–59, 2015, doi: 10.3390/coatings6010001.
4. H. El Knidri, R. Belaabed, A. Addaou, A. Laajeb and A. Lahsini, “Extraction, chemical modification and characterization of chitin and chitosan,” *Int. J. Biol. Macromol.*, vol. 120, pp. 1181–1189, 2018, doi: 10.1016/j.ijbiomac.2018.08.139.
5. M. Triunfo, E. Tafi, A. Guarnieri, R. Salvia, C. Scieuzo, T. Hahn, S. Zibek, A. Gagliardini, L. Panariello, M. B. Coltelli, A. De Bonis and P. Falabella, “Characterization of chitin and chitosan derived from Hermetia illucens, a further step in a circular economy process,” *Sci. Rep.*, vol. 12, no. 1, pp. 1–17, 2022, doi: 10.1038/s41598-022-10423-5.
6. M. Jones, M. Kujundzic, S. John and A. Bismarck, “Crab vs. Mushroom: A review of crustacean and fungal chitin in wound treatment,” *Mar. Drugs*, vol. 18, no. 1, 2020, doi: 10.3390/md18010064.
7. M.B. Coltelli, P. Morganti, V. Castelvetro, A. Lazzeri, S. Danti, B. Benjelloun-Mlayah, A. Gagliardini, A. Fusco and G. Donnarumma, “Chitin Nanofibril-Nanolignin Complexes as Carriers of Functional Molecules for Skin Contact Applications,” pp. 1–23, 2022.
8. S. Danti, L. Trombi, A. Fusco, B. Azimi, A. Lazzeri, P. Morganti, M.B. Coltelli and G. Donnarumma, “Chitin nanofibrils and nanolignin as functional agents in skin regeneration,” *Int. J. Mol. Sci.*, vol. 20, no. 11, 2019, doi: 10.3390/ijms20112669.
9. L. Panariello, M. B. Coltelli, M. Buchignani and A. Lazzeri, “Chitosan and nano-structured chitin for biobased anti-microbial treatments onto cellulose based materials,” *Eur. Polym. J.*, vol. 113, no. October 2018, pp. 328–339, 2019, doi: 10.1016/j.eurpolymj.2019.02.004.
10. P. Cinelli, M. B. Coltelli, N. Mallegni, P. Morganti and A. Lazzeri, “Degradability and sustainability of nanocomposites based on polylactic acid and chitin nano fibrils,” *Chem. Eng. Trans.*, vol. 60, no. September, pp. 115–120, 2017, doi: 10.3303/CET1760020.
11. J. Wu, K. Zhang, N. Girouard and J. C. Meredith, “Facile route to produce chitin nanofibers as precursors for flexible and transparent gas barrier materials,” *Biomacromolecules*, vol. 15, no. 12, pp. 4614–4620, 2014, doi: 10.1021/bm501416q.
12. S. Ifuku, M. Nogi, M. Yoshioka, M. Morimoto, H. Yano and H. Saimoto, “Fibrillation of dried chitin into 10-20 nm nanofibers by a simple grinding method under acidic conditions,” *Carbohydr. Polym.*, vol. 81, no. 1, pp. 134–139, 2010, doi: 10.1016/j.carbpol.2010.02.006.
13. Y. Fan, T. Saito and A. Isogai, “Individual chitin nano-whiskers prepared from partially deacetylated α-chitin by fibril surface cationization,” *Carbohydr. Polym.*, vol. 79, no. 4, pp. 1046–1051, 2010, doi: 10.1016/j.carbpol.2009.10.044.

Proceedings of the SICT/PlasmaTech/Tribology 2022 Joint International Conference
Barcelona, Spain – April 27 – 29, 2022
DOI: https://doi.org/10.26799/cp-sict-plasmatech-tribology-2022

Evaluation of Galvanic Anodes Capacity as Per NACE TM0190-98 Test Methods

Nayif A ALRrasheedi [1], Sultan ALMutairi [2]

[1] Saudi Aramco, Research & Development Centre, Dhahran, Saudi Arabia, nayif.rasheedi@aramco.com

[2] Saudi Aramco, Research & Development Centre, Dhahran, Saudi Arabia sultan.mutairi.1@aramco.com

Abstract

NACE-TM-0190 method was implemented to evaluate Aluminium, Zinc & High Temperature Zinc galvanic anodes used for cathodic protection system. The test was conducted by passing a fixed direct current through test cells electrically connected in series. The test cell is made of carbon steel and it is the cathode in the electrical circuit. Each test cell contains an electrolyte for current flow which is seawater. The fixed direct current flows for a period of 14 days during which the anodes are partially consumed. The ampere-hour obtained per unit mass of anode lost is calculated. The value is compared to that of pure anode metal to determine the percentage efficiency of each tested galvanic anode

Keywords: galvanic anodes Anode, Electrochemical Performance, Efficiency.

1. Introduction

Testing anode castings for quality and output is an essential part of the bulk anode manufacturing process. The testing should be carried out as part of the manufacturing process control regime. The testing should also be conducted in accordance with the industry standards established by NACE in the testing method document NACE TM 0190.

Part of the qualification process is to test samples of their anodes against 17-SAMSS006 requirements including expected life time. These anodes are rated for long term life and any substandard anodes will end up affecting the integrity and safety of company assets, people and environment in addition to the installation and operations interruptions. A zinc anode is a type of sacrificial anode used to prevent corrosion through cathodic protection. Zinc anodes are the preferred choice in metal alloys for saltwater applications that need a sacrificial anode, because the alloy is less resistant to the saltwater's electrolytes. To counteract galvanic corrosion is to add a third metal into the circuit, one that is quicker than the other two to give up its electrons. All metals immersed in an electrolyte produce an electrical voltage. The most active metal (zinc) becomes the anode to the others and sacrifices itself by corroding to protect the cathode. The zinc stops the oxidation happening to the other metal part as the zinc dissolves away and loss weight. [1]

Due to the special working environment of oil and gas offshore engineering, when using a coating to protect the steel structure, a sacrificial anode must be used as an auxiliary anti-corrosion protection method. NACE TM 0190.and other international standards or recommended practices are usually selected to draft technical specifications for cathodic protection of offshore engineering projects. These technical specifications cover similar criteria to ensure the quality of sacrificial anodes for Cathodic Protection such as technical requirements, inspection, chemical composition and electrochemical performance. However, each project has its own complexity and performance requirement, due to the different operating condition (environment) of the assets and the actual usage condition of the sacrificial anode. Therefore, the quality and performance parameters of the sacrificial anode need to be stated carefully and in detail, in the specification to cover all the potential risks involved in the project. At present, the design (service) life of offshore oil engineering equipment/structure is over 25 years, similar to the design life of sacrificial anodes (25 years). Therefore, ensuring the long-term performance of sacrificial anodes is an important factor to ensure the safety/integrity of offshore assets. [2]

the current international codes & standards such as NACE TM0190-98, has provided quality control requirements at the casting stage, such as: anode size, weight, appearance, internal defects, chemical composition, electrochemical capacity. However, in engineering practice, we often find that the actual performance of the sacrificial anode does not meet the project's expectations.

DOI: https://doi.org/10.26799/cp-sict-plasmatech-tribology-2022

2. Experimental Procedure

SALAM 220-10 methods provide detailed instructions for the laboratory evaluation of anodes for use in cathodic protection systems. The procedure is basically derived from NACE TM0190-98 standard test method. The SALAM modifies specific portions of TM090-98 to align with the test apparatus and procedures used in Saudi Aramco facilities. However, NACE TM0190-98 is the original reference and it should be consulted for any additional questions. [3]

The test cell is made of carbon steel and it is the cathode in the electrical circuit, Figure 1. Electrochemical galvanic test is used to measured galvanic potential of each anode coupled with carbon steel cell with respect to the control anode immersed in ASTM D1141 "Substitute Ocean Water" at 1220 F/500 C. The bulk synthetic seawater shall be mixed for a minimum of 24 h prior to the beginning of the test. Each test cell also contains an electrolyte for current flow (seawater). The test cells shall be filled with seawater to within 1.3 cm. The test method is conducted by passing a fixed direct current through test cells electrically connected in series. Each test cell contains a pre-weighed anode test coupon. Zinc anode samples conforming to ASTM B 418 Type I (Vol 02-Q4) should be used in the test as a reference material. Instructions for cleaning zinc samples before testing are given in ASTM G 1. The fixed direct current flows for a period of 14 days during which the anodes are partially consumed. The voltage and resistance adjusted to give a current of 24 ±0.2 mA as measured by the milliammeter. The current should be checked periodically for drift throughout the test and adjusted to 24 ±0.2 mA. The potentials and the temperature of the seawater electrolyte shall be recorded. After the test, the coupons are cleaned and weighed again to determine their weight loss. The total ampere hour of current flowing for the 14 days period is a known quantity. Using these two values, the ampere-hour obtained per unit mass of anode lost is calculated. This value is compared to that of pure anode metal to determine the percentage efficiency of each tested galvanic anode [4]

Calculations Method

Coupon ampere-hour / kilogram = (12.9242 ampere-hour/kilogram) / (coupon weight loss, kilogram)

pure Zinc at an assumed 100 % efficiency has a capacity of 819.7 ampere-hours / kilogram

calculation of Zinc % efficiency = (coupon ampere-hour/kilogram) / (819.7 ampere-hour/ kilogram) * 100

Electrochemical galvanic test was used to measured galvanic potential of each anode coupled with carbon steel cell with respect to SCE immersed in sea water in accordance to ASTM D1141 for 14 days exposure.

In collaboration with metallurgy lab spark optical emission spectroscopy was used to analyses the chemical compositions of Aluminum, Zinc & High Temperature Zinc alloys. [4]

3. Results and Discussion

The average efficiency calculated for the set of "(Aluminium, Zinc, and High temperature Zinc) anodes were 92%, 99%, and 97% respectively. Table 1 summarize the efficiency and the average current capacity results and show that the average capacity, Ampere-Hour/Kilogram for anodes are: Aluminium (2746), Zinc (813), and for Zinc -high temperature is about 795.The sacrificial anodes were immersed in sea water in accordance to ASTM D1141 standard and the open circuit potential (OCP) reached the stability at the beginning of the experiment. The value of the steady state OCP are shown in Figure 2. Spark optical emission spectroscopy identified the composition of the anodes. The chemical compositions of these anode samples are listed in Table 2.

4. Conclusion

The average efficiency calculated for the set of "(Aluminium, Zinc, and High temperature Zinc) anodes were 92%, 99%, and 97% respectively and the open circuit potential (OCP) for (Aluminium, Zinc, and High temperature Zinc) reached the stability at the beginning of the experiment

5. References

1. 17-SAMSS-006 Galvanic Anodes for Cathodic Protection

DOI: https://doi.org/10.26799/cp-sict-plasmatech-tribology-2022

2. NACE TM0190 Standard Test Method Impressed Current Test Method for Laboratory Testing of Aluminum Anodes
3. SALAM 220-10 methods provide detailed instructions for the laboratory evaluation of anodes for use in cathodic protection systems
4. ASTM D1141 (latest revision), "Standard Practice for the Preparation of Substitute Ocean Water

6. Figures and Tables

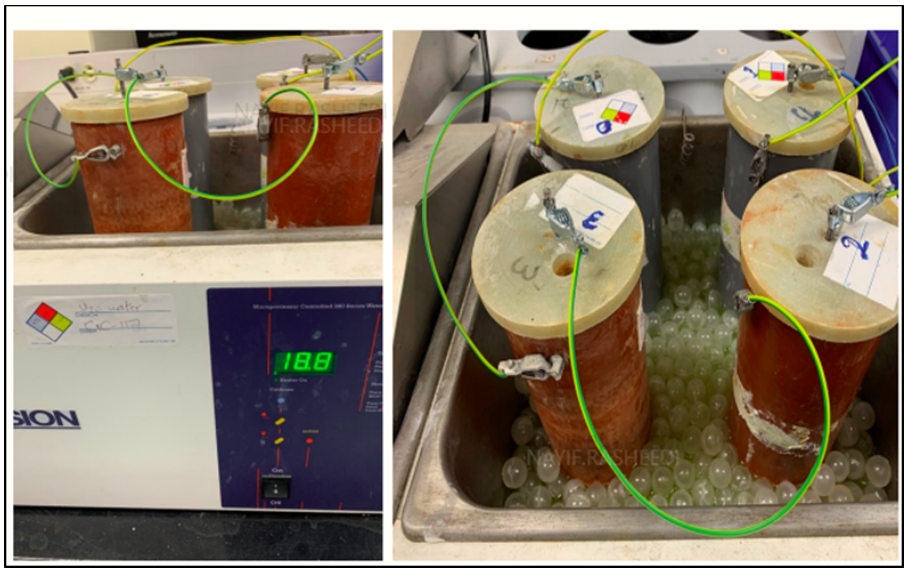

Figure. 1: Test cell is made of carbon steel used in the experiment.

Table 1: Summarizes the efficiency and the average current capacity results of (Aluminium, zinc and zinc high temperature

Anode Type	Anode No	Initial Weight, (g)	Final Weight, (g)	Weight Loss, (g)	Capacity, Ampere-Hour/Kg	Average Capacity, Ampere-Hour/Kg	% Efficiency
Aluminium	1 (S)	52.6938	47.9364	4.7574	2717	2746	92
	2	52.3753	47.7075	4.6678	2769		
	3	52.5028	47.8087	4.6941	2753		
Zinc	4 (S)	133.7264	117.5813	16.1451	801	813	99
	5	133.5283	117.767	15.7613	820		
	6	135.3465	119.5405	15.806	818		
Zinc (high temperature)	7 (S)	135.0797	118.6514	16.4283	787	795	97
	8	131.3137	114.7075	16.6062	778		
	9	134.5776	118.822	15.7556	820		

DOI: https://doi.org/10.26799/cp-sict-plasmatech-tribology-2022

Table 2: Chemical composition of Aluminium, Zinc, and High temperature Zinc

Element	Aluminium	Zinc	High Temperature Zinc
Zn	5.638	99.81	96.237
Fe	0.283	0.164	0.12
Si	0	0	0
Cu	0.014		0
Mn	0	0	0
Mg	0	0	0
Cr	0	0	0
Ni	0	0	0
Ti	0	0	0
Be	0	0	0
Pb	0	0	0
Sn	0	0	0
V	0	0	0.789
Zr	0	0	0
Al	93.172		0
Mo	0	0	0
Na	0	0	0
P	0	0	0
Sb	0	0	0
Sr	0	0	0
Tl	0	0	1.748

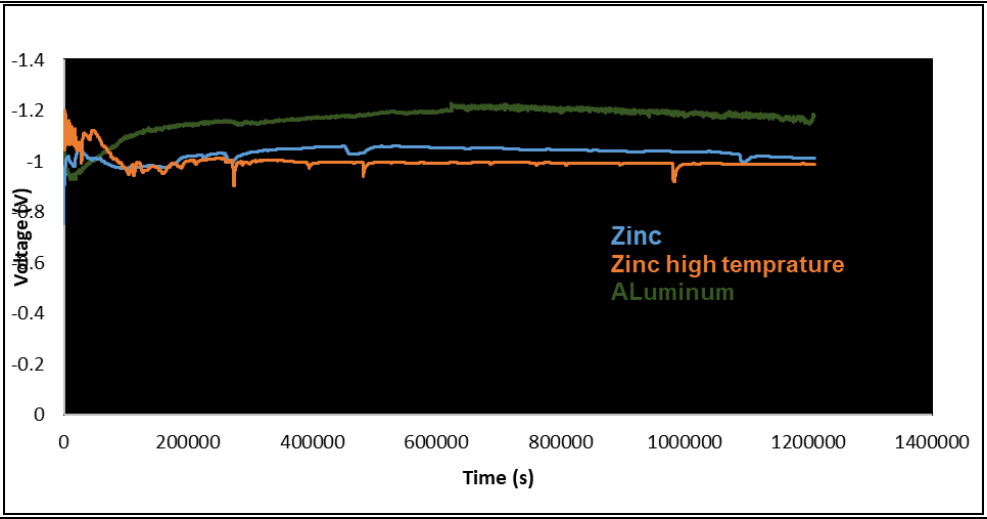

Figure 2: Open circuit potential of Aluminium, Zinc, and High temperature Zinc VS. SCE

Proceedings of the SICT/PlasmaTech/Tribology 2022 Joint International Conference
Barcelona, Spain – April 27 – 29, 2022
DOI: https://doi.org/10.26799/cp-sict-plasmatech-tribology-2022

Behaviour of Electric Arc in Plasma-Chemical Reactor During Hazardous Waste Processing

V. Grigaitienė, D. Gimžauskaitė, V. Valinčius, R. Kėželis, R. Uscila, Ž. Kavaliauskas

Plasma Processing Laboratory, Lithuanian Energy Institute
Breslaujos str. 3, LT-44403 Kaunas, Lithuania, Viktorija.Grigaitiene@lei.lt

Abstract

The atmospheric pressure plasma technology is an innovative technique for manufacturing novel and better materials, modifying surfaces, hazardous waste treatment, etc. A novelty of this research is the employment of atmospheric pressure direct current (DC) plasma torch with a free burning electric arc for waste treatment in a volume plasma-chemical reactor. Plasma equipment with a prototype volumetric plasma reactor for waste destruction and decomposition has been designed and used in Lithuanian Energy Institute, Plasma Processing Laboratory. This paper presents the operational characteristics and optical images of DC electric arc behaviour in the plasma-chemical reactor during hazardous waste processing. The treatment process of selected mineral waste materials (clay and phosphogypsum, clay and hydroquinone mixtures) was realized, and characteristics of high-temperature plasma flow were investigated. The waste treatment process and the operating electric arc's behaviour inside the reactor were recorded using a high-speed camera. It was established that the electric arc's formation and movement are most likely at the location where the thinnest layer of the waste material is located.

Keywords: plasma torch, waste treatment, volume reactor, hazardous waste

1. Introduction

The problem of waste generated by the development of industrial production and advanced modern technologies is becoming increasingly important. As the consumption of goods and services grows, increasing amounts of secondary raw materials such as various plastics, rubber, medical and chemical waste, etc., are generated [1–2]. Today's scientists have new challenges related to the sustainable use of waste and recyclable products, as well as the neutralization and conversion of hazardous waste into environmentally friendly materials. Therefore, there is an increasing focus on using secondary raw materials and waste as alternative energy sources: incineration, neutralization or other waste recycling methods [3–4]. The process temperature of most of these methods reaches only 1500 ºC. These temperatures are insufficient for neutralization or recycling processes for hazardous wastes such as furans, chlorine or sulfur compounds, and various carbon derivatives. In order to neutralize or recycle hazardous and hardly breaking waste, the process temperature must reach at least 1800 ºC and above [5–6]. It is not possible to achieve such ambient temperatures using traditional methods. The plasma waste decomposition method is characterized by extremely high decontamination efficiency (99.99%), high temperatures (around 13,000 ºC in the arc zone), high energy density, fast process control, and more environmentally friendly than traditional waste treatment methods. However, for the waste neutralization process to be fully realized in a plasma environment, it is necessary that materials remain in the plasma environment for at least 1–2 s. In order to carry out these tasks, volume plasma-chemical reactors are commonly used. While using plasma neutralization technologies, the end products of waste neutralization are usually gas and vitrified slag.

2. Experimental setup

Plasma technology with a prototype volumetric plasma-chemical reactor to melt and decompose different waste materials has been used in this research. The main part of the plasma-chemical reactor is a transferred arc plasma torch. This device as a prototype was developed at the Plasma Processing Laboratory of the Lithuanian Energy Institute. The bottom of the reactor was made of conductive graphite, which also played the role of an anode. The electric arc in the volume reactor burned chaotically. The power of the plasma torch was up to 40 kW, and the discharge current was 160 A. A schematic diagram of the plasma-chemical reactor is shown in Figure 1. Plasma forming gas (air) was supplied with a flow rate of 0,8 g/s. The recycled mixtures: a) clay and hydroquinone (composition of 25% hydroquinone and 75% clay) and b) clay and phosphogypsum (25 % phosphogypsum and 50 % clay) were injected into a plasma-chemical reactor through the input nozzle. Clay

DOI: https://doi.org/10.26799/cp-sict-plasmatech-tribology-2022

powder was chosen as a carrier, and hydroquinone or phosphogypsum was chosen as neutralized waste. With a waste content of more than 25%, there are technical problems with mixture dosing as it becomes sticky. The distance between the plasma torch and the top layer of conductive material was 10 cm, waste feeding rate was 3 g/s.

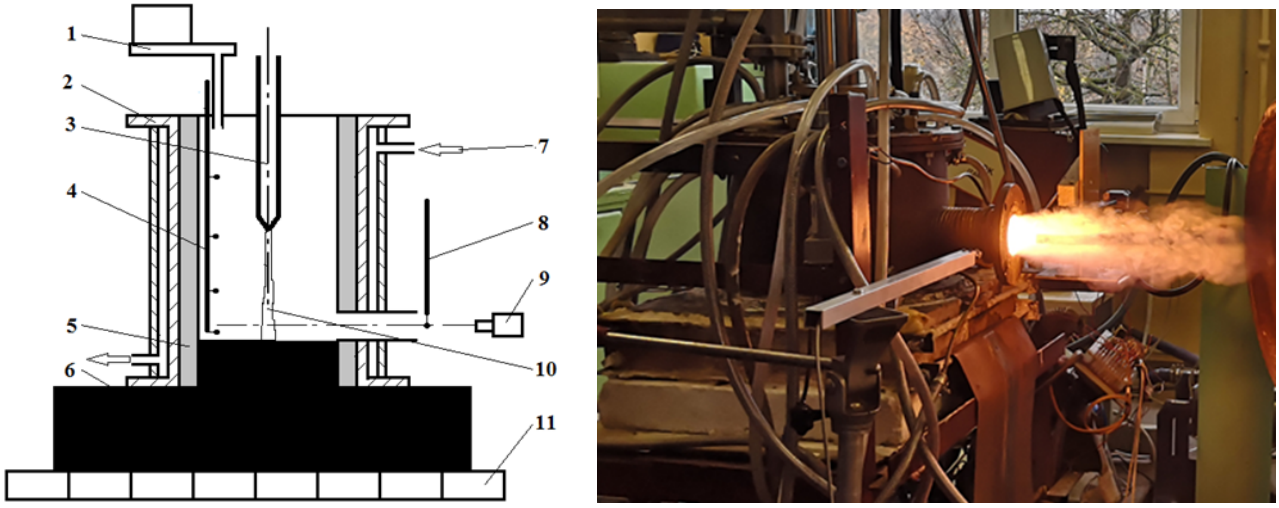

Figure 1: The schematic representation of plasma-chemical reactor. 1 – raw material input, 2 – cooled block, 3 – plasma torch, 4 – probe for gas temperature measurements, 5 – inner high-temperature insulation layer, 6 – graphite anode, 7 – cooling water in, 8 – probes for outlet gas temperature, content and spectra measurements, 9 – high-speed camera, 10 – arc column, 11 – insulating base.

The investigation of the formation of multiphase flow parameters has been performed experimentally. A high-speed camera (12-bit CMOS camera Phantom Miro M310) equipped with a zoom lens and a neutral density UV filter was used to visualize the plasma flow and instantaneous imaging of the plasma arc. During the plasma-chemical waste treatment process, a gas analyzer SWG 300-1 was used to analyze the composition of the emitted gas.

3. Results

A discharge of the electric arc is generated between the conductive bottom of the reactor (which acts as an anode) and the plasma torch. Figure 2 shows plasma flow images obtained using a high-speed Phantom video camera. The recorded images showed that the electric arc of the ionized gas moves chaotically inside the plasma-chemical reactor's chamber. Figure 2 (case a–b) shows the discharge of an electric arc when no waste material is treated inside the plasma-chemical reactor. It was observed that the electric arc moves over the entire surface of the graphite anode. Figure 2c–d shows the electric arc discharge when the clay is mixed with hydroquinone and was supplied to the volumetric reactor on the graphitic bottom. An electric arc occurs where the lowest energy consumption is required to form it. Figure 2e–f shows the electric arc discharge when the clay is mixed with phosphogypsum powder and processed. After the visual analysis of plasma arc behaviour, it can be seen the electric arc moves chaotically when the treated material interacts with the gas flow. The particles of the raw waste mixture are fed by a motorized screw feeder onto the surface of the anode, which is covered with a layer of melt of uneven thickness. Such types of waste are poor conductors, and the probability of electric arc formation is the greatest at the point where the particle layer is melted to a liquid and thinnest. The thickness of the layer is constantly changing and simultaneously influences the energy characteristics of the electric arc's formation. The life span of the plasma-chemical reactor decreases and the energy characteristics of the electric arc formation vary.

DOI: https://doi.org/10.26799/cp-sict-plasmatech-tribology-2022

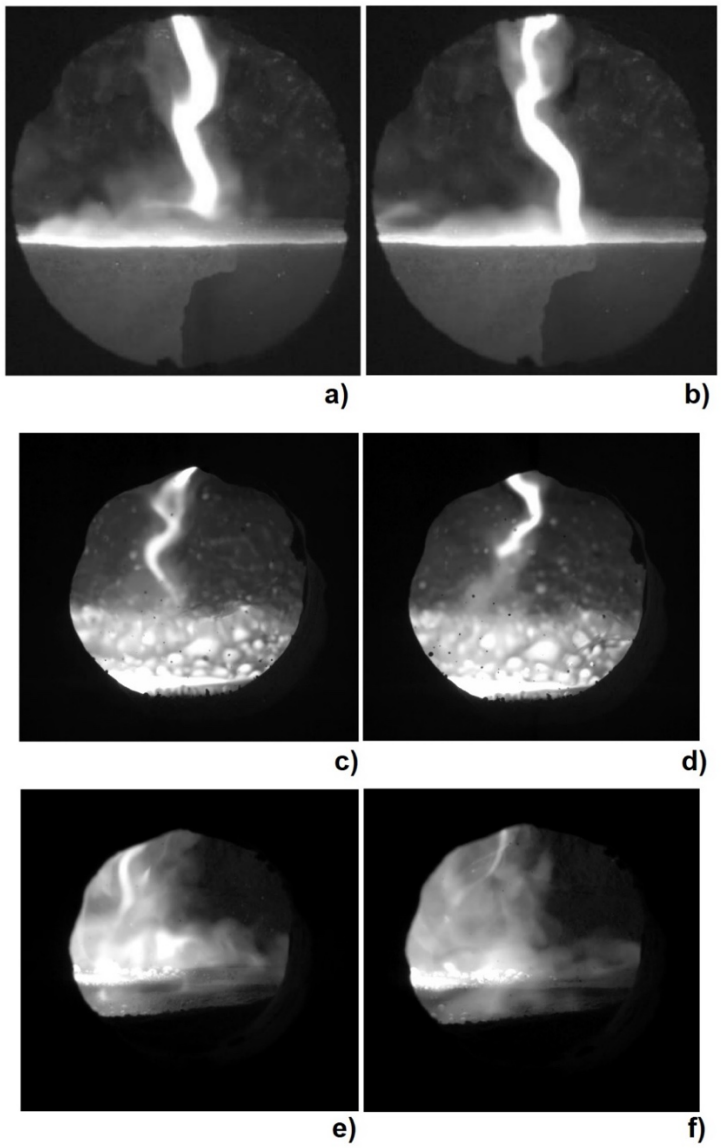

Figure 2. High-speed video camera images with a frame exposure time of 1 μs and frames per second rate of 2000 fps: when (a–b) – no waste material to be processed in the volume reactor; (c-d) – the reactor when the clay and hydroquinone mixture is treated; (e-f) – the reactor when the clay and hydroquinone mixture is treated.

By recycling phosphogypsum and hydroquinone waste in a plasma chemical reactor, gaseous products were produced that can be used in the energy sector. The chemical properties and flow rate of gases emitted during the decontamination process has been evaluated and presented in Table 3. The wastes that require recycling contain compounds with large amounts of carbon, hydrogen or oxygen, which, when broken down into their primary components, turn into flammable gases that react with oxygen to become a water vapor or carbon dioxide.

Table 3. Outlet gas composition emitted during the plasma waste treatment.

	O_2,%	**CO_2,%**	**CO,%**	**H_2,%**	**NO, %**	**NO_2, %**	**SO_2, %**	**C_3H_8, %**
Clay + phosphogypsum	17,52	3,51	0	0	0	0	0	0
Clay + hydroquinone	0,53	6,54	21,8	5,8	0	0	0	0

Figure 3 shows an image of a material already processed during the plasma treatment, and a melted slag is gained as a final product. The surface structure comprises various irregularly shaped microstructures.Melting,

DOI: https://doi.org/10.26799/cp-sict-plasmatech-tribology-2022

boiling and evaporation of the feedstock take place inside the reactor during the plasma chemical process and the material amount is reduced 10-12 times in volume by melting or vaporization.

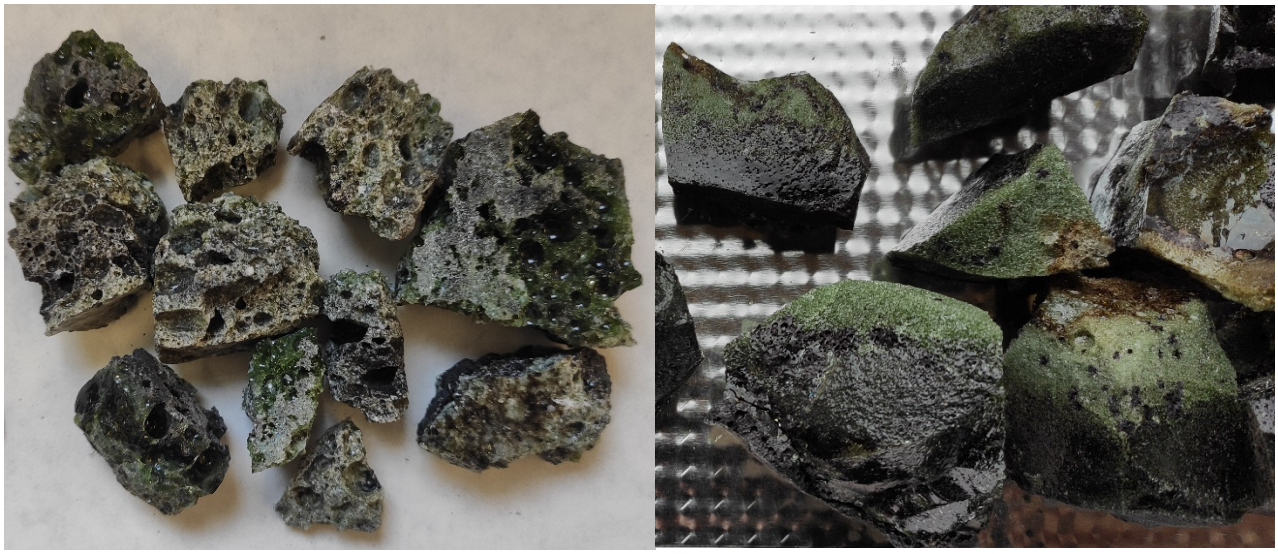

Figure 3. Vitrified slag after plasma waste treatment. a) clay and hydroquinone slag, b) clay and phosphogypsum slag.

4. Conclusion

The hard mineral wastes were treated in a pilot-scale plasma-chemical reactor with a plasma torch at a power of 40 kW. The plasma torch has a plate-shaped graphite anode in order to maximize process efficiency. The novelty of the research is the use of a plasma torch with free burning electric arc for hazardous waste treatment. The characteristics of the atmospheric pressure air plasma torch and its application for mineral waste treatment were investigated. The power range of the plasma torch is 40 – 60 kW, and the arc current is 150 – 270 A. Technological and temperature modes of such plasma chemical reactor allow decomposition of waste and obtain new products with environmentally friendly properties. The chaotical movement of the electric arc is the greatest at the location where the thinnest layer of the melted waste material is located.

Acknowledgements

This research (Project no. 01.2.2-LMT-K-718-01-0069) is funded by the European Regional Development Fund according to the supported activity' Research Projects Implemented by World-class Researcher Groups' under measure no. 01.2.2-LMT-K-718.

References

1. Z. Peng, G.Ni, Y. Jiang, L. Chen, et al. Destruction of inorganic municipal solid waste incinerator fly ash in a DC arc plasma furnace. J Hazard Mater. 2010, 181, pp.580–585.
2. A. Soltani, K. Hewage, B. Reza, R. Sadiq. Multiple stakeholders in multi-criteria decision-making in the context of municipal solid waste management: a review. Waste Management 35, 2016, pp. 318-328.
3. P. Kumar, N. K. Jain, Effect of material form on deposition characteristics in micro-plasma transferred arc additive manufacturing process. CIRP J. Manuf. Sci. Technol. 2020, 30, pp. 195–205.
4. J. Song, B. Kim, D. Park, J.H. Kim, Fabrications of spherical alumina particles by controlling process parameters in a transferred arc plasma system. Ceram. Int. 2020, 46, pp. 21225–21232.
5. R. Zhang, F. Jiang, S. Chen, Droplet transfer behaviour in twin-body plasma arc welding. J. Manuf. 2019, 41, pp. 330–336.
6. M. Rajasekhar, N.V. Rao, G.C. Rao, et al. Energy Generation from Municipal Solid Waste by Innovative Technologies – Plasma Gasification. Procedia Mater. Sci. 2015, 10, pp. 513–518.

Proceedings of the SICT/PlasmaTech/Tribology 2022 Joint International Conference
Barcelona, Spain – April 27 – 29, 2022
DOI: https://doi.org/10.26799/cp-sict-plasmatech-tribology-2022

The Influence of RF- power on Structure and Photocatalytic Properties of thin PEALD ZnO Films Deposited at Room Temperature

Daria Jardas[1,2], Robert Peter[1,2], Marko Perčić[2,3], Krešimir Salamon[4], Aleš Omerzu[1,2], Mladen Petravić[1,2]

[1] University of Rijeka, Faculty of Physics, Radmile Matejčić 2, 51000 Rijeka, Croatia, daria.jardas@uniri.hr, rpeter@uniri.hr, aomerzu@uniri.hr, mpetravic@uniri.hr
[2] University of Rijeka, Centre for Micro- and Nanosciences and Technologies, Radmile Matejčić 2, 51000 Rijeka, Croatia
[3] University of Rijeka, Faculty of Engineering, Vukovarska 58, 51000 Rijeka, Croatia, mpercic@riteh.hr
[4] Ruđer Bošković Institute, Bijenička cesta 54, 10000 Zagreb, Croatia, Kresimir.Salamon@irb.hr

Abstract

The photocatalytic activity of thin ZnO films deposited by plasma-enhanced atomic layer deposition at room temperature was investigated for different radio- frequency (RF) powers applied during synthesis. The films prepared with higher plasma power show higher photocatalytic activity. Structural and optical measurements were performed to determine the origin of their properties. All the films prepared were predominantly amorphous. However, the films prepared with higher plasma power show a more ordered structure.

Keywords: ZnO, thin films, plasma- enhanced atomic layer deposition, RF power, photocatalysis

1. Introduction

Zinc oxide (ZnO) is a semiconductor with a wide, direct band gap (~ 3.37 eV) and an exciton binding energy of 60 meV [1]. Among many other applications, ZnO has been investigated for its potential use in photocatalytic degradation of organic pollutants [2]. As a photocatalyst, ZnO was initially used in the form of powder [3], but recently, efforts have been invested in the synthesis of ZnO thin films to avoid the technically demanding removal of the used powder photocatalyst from the solution [4]. Thin ZnO films can be synthesised by various methods, such as chemical vapor deposition (CVD) [5], molecular beam epitaxy (MBE) [6], pulsed laser deposition (PLD) [7], sputtering [8] or atomic layer deposition (ALD) [9]. Among these methods, only ALD is characterised by both relatively low processing temperature (< 250 ºC), precise control of thickness and structure, large-area uniformity, and high quality of films [10]. In conventional thermal ALD, the surface reactions are thermally driven and the reactants are in a gaseous state [9]. Therefore, the properties of the thin ZnO films strongly depend on the substrate temperature during deposition. The range of ALD deposition temperatures for ZnO is between 60 ºC and 250 ºC, while the best photocatalytic properties are obtained for films deposited above 150 ºC [11, 12] making the deposition unsuitable on thermally sensitive organic and biological substrates. A further upgrade of the thermal ALD method is plasma-enhanced atomic layer deposition (PEALD), in which the activation of precursors is assisted by plasma that requires lower synthesis temperature than in conventional, thermal ALD [13]. In addition, for some applications, the ZnO films synthesised by PEALD exhibit superior properties in comparison with the ALD films. For example, the films deposited at 80 ºC have 10 times higher photocatalytic activity than the films synthesised at the same temperature using ALD [14]. The PEALD synthesis is also possible at room temperature [15, 16], which allows the use of temperature-sensitive substrates and opens numerous new applications. An important parameter in the PEALD technique, which also affects the material properties, is the plasma RF power [16]. The aim of the presented research is to investigate the photocatalytic activity of PEALD ZnO thin films at room temperature and its dependence on RF power.

DOI: https://doi.org/10.26799/cp-sict-plasmatech-tribology-2022

2. Materials and Methods

2.1. PEALD synthesis

PEALD deposition of thin ZnO films was performed in Beneq TFS 200 system at room temperature. Three types of substrates were used: microscope coverslips (for photocatalytic measurements), fused silica wafers (for optical measurements) and Si(100) wafers (for structural characterization with Grazing Incidence X-ray Diffraction (GIXRD) and Atomic Force Microscopy (AFM) measurements). Diethylzinc (DEZ, STREM Chemicals) and oxygen plasma were used as zinc and oxygen precursors, respectively, while high purity nitrogen was applied as purging gas. A PEALD cycle consisted of a 250 ms DEZ pulse, 2.5 s nitrogen purge, 3 s O_2 plasma pulse, followed by 6 s N_2 purge. The PEALD reactor is equipped with a capacitively coupled plasma unit with a 13.56 MHz RF power source. Plasma powers of 100 W, 150 W, 200 W or 250 W were used during the depositions. The number of cycles varied from 100 cycles (for 100 W) to 275 cycles (for 250 W), depending on the growth rate. In addition, thermal ALD was performed at a temperature of 200 ºC in the same reaction chamber and on same substrates, again with DEZ as zinc precursor and nitrogen as a purge gas, but with deionized H_2O as oxygen precursor instead of O_2 plasma. The deposition consisted of 430 cycles, and the pulsing cycles of 200 ms DEZ, 1 s N_2, 180 ms H_2O, and 1 s N_2.

2.2 Thin film characterization

The crystalline structure was determined from GIXRD measurements using an X-ray diffractometer (Siemens D5000) with Cu-K_α radiation in grazing mode at a fixed grazing incidence angle of 1 º. The optical absorption of the thin PEALD ZnO films deposited on fused silica plates was measured with a UV-Vis spectrophotometer (Thermo Scientific, Evolution 201) in the spectral range of 200 - 800 nm. The scans of the surface topology of the analysed samples were obtained using the AFM (Bruker Dimension Icon) in tapping mode. The photocatalytic activity of the ZnO films was measured by monitoring the photodegradation of methylene blue (MB) in distilled water under UV light (OSRAM Puritec HNS G5 6 W). Glass slides (3 cm x 1 cm) with deposited thin ZnO films were illuminated for 16 hours outside the MB solution and illuminated for 7 hours in 15 mL MB water solution with an initial concentration of 1.35 x 10^{-5} M . The absorption spectrum was recorded every 60 minutes and the change in intensity of the characteristic MB absorbance peak at 664 nm was recorded.

3. Results and discussion

In Fig. 1 we show an example of the difference in crystallinity of thin ZnO films deposited by PEALD at room temperature and RF power of 100 W and deposited by thermal ALD at 200 ºC, as determined by GIXRD measurements. The diffraction pattern of the ALD film shows peaks at typical positions for crystalline ZnO, while the diffraction pattern of the RT PEALD film is a very broad line with no observable sharp diffraction peaks that is characteristic for an amorphous material. Other PEALD ZnO films deposited at room temperature for the other values of RF power employed in this study show similar GIXRD patterns.

DOI: https://doi.org/10.26799/cp-sict-plasmatech-tribology-2022

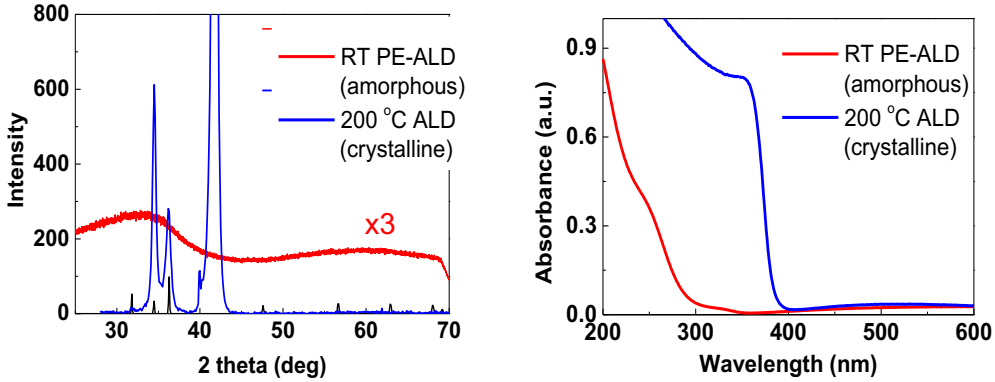

Fig. 1: a) GIXRD patterns for room-temperature PEALD and 200 ºC thermal ALD ZnO thin films.b) UV-Vis spectra of thin ZnO films deposited by PEALD at room temperature and RF power of 100 W and by thermal ALD at 200 ºC.

Therefore, we can conclude that the PEALD ZnO films deposited at room temperature are predominantly amorphous. The same two samples (RT PEALD with 100 W and ALD at 200 ºC) were analysed by UV-Vis spectroscopy. Instead of sharp increase in optical absorptivity at the band edge (380 nm) observed in the crystalline film, optical absorptivity curve for the RT PEALD film gradually increases for wavelengths < 350 nm (see Fig. 1b). Such stretched optical absorption is typical for amorphous semiconductors.

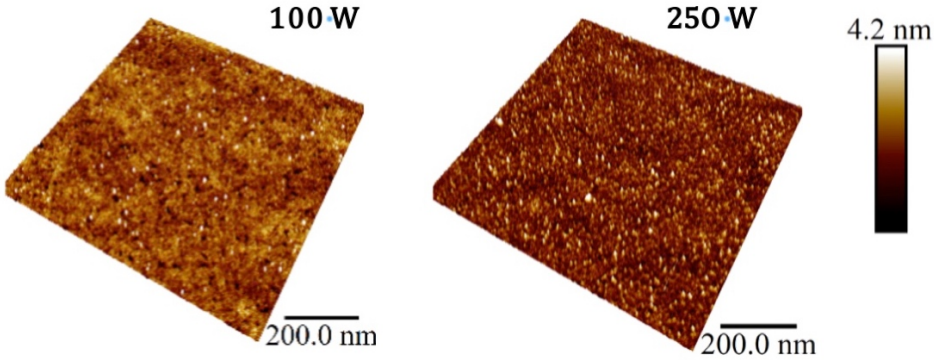

Fig. 2: AFM micrographs of thin PEALD ZnO films deposited at room temperature using 100 W (left) and 250 W (right) RF power.

The representative AFM results of the surface topology and roughness study are compared in Fig. 2 and listed in Table 1 for the thin PEALD ZnO films deposited at room temperature with RF powers of 100 W and 250 W. Both films are primarily amorphous, but show some individual crystalline grains on the surface. The film deposited with 250 W RF power has a higher surface concentration of slightly larger grains.

Table 1: Results of the roughness measurement.

RF power (W)	R_q (nm)	R_a (nm)	R_{max} (nm)
100	0.528	0.383	9.20
250	0.560	0.425	7.88

DOI: https://doi.org/10.26799/cp-sict-plasmatech-tribology-2022

Finally, the histograms of photocatalytic efficiency after 7 hours of UV illumination of thin PEALD ZnO films deposited with different RF powers are shown in Fig. 3. The percentage of degraded MB is significantly higher for thin films deposited with RF power higher than 200 W than for films deposited with lower RF power.

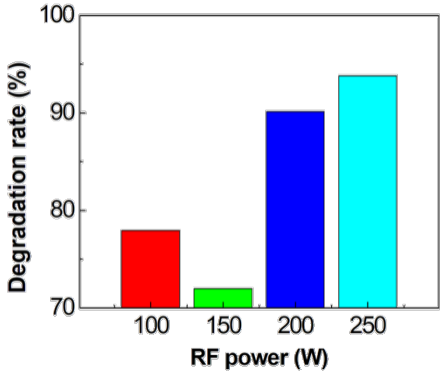

Fig. 3: Histograms of the photocatalytic degradation efficiency of thin PEALD ZnO films deposited with RF powers ranging from 100 W to 250 W after 7 hours of UV irradiation.

4. Conclusion

From the presented results, we can conclude that RF plasma power higher than 200 W is reqired for thin ZnO films synthesised by PEALD at room temperature to achieve the better photocatalytic activity. Structural analysis has shown that the films deposited by RF power higher than 200 W have a slightly higher degree of crystallinity, but are predominantly amorphous, in contrast to the polycrystalline films deposited by thermal ALD at 200 ºC.

Acknowledgements

This study was supported by the University of Rijeka under the project number 18-144. The authors would like to acknowledge Karlo Veličan for his special efforts in cleaning the reactor chamber between syntheses.

References

1. Ü. Özgür, et al., “A comprehensive review of ZnO materials and devices,” *J. Appl. Phys*., vol. 98, no. 4, p. 041 301, 2005.
2. H. Kisch, *Semiconductor Photocatalysis: Principles and Applications*, 1st ed. Wiley-VCH, 2015.
3. A. Sharma, P. Rao, R. Mathur, and S. C. Ameta, “Photocatalytic reactions of xylidine ponceau on semiconducting zinc oxide powder,” J. Photochem. Photobiol. A: Chem., vol. 86, no. 1, pp. 197–200, 1995.
4. L. Roselin, G. Rajarajeswari, R. Selvin, V. Sadasivam, B. Sivasankar, and K. Rengaraj, “Sunlight/ZnO-mediated photocatalytic degradation of reactive red 22 using thin film flat bed flow photoreactor,” Solar Energy, vol. 73, no. 4, pp. 281–285, 2002.
5. M. Purica, E. Budianu, E. Rusu, M. Danila, and R. Gavrila, “Optical and structural investigation of ZnO thin films prepared by chemical vapor deposition (CVD),” *Thin Solid Films*, vol. 403-404, pp. 485–488, 2002, *Proceedings of Symposium P on Thin Film Materials for Photovoltaics.*
6. Y. Chen, et al., “Plasma assisted molecular beam epitaxy of ZnO on c-plane sapphire: Growth and characterization,” *J. Appl. Phys*., vol. 84, no. 7, pp. 3912–3918, 1998.
7. E. M. Kaidashev, et al., “High electron mobility of epitaxial ZnO thin films on c-plane sapphire grown by multistep pulsed-laser deposition,” *Appl. Phys. Lett*., vol. 82, no. 22, pp. 3901–3903, 2003.
8. F. Quaranta, A. Valentini, F. R. Rizzi, and G. Casamassima, “Dual-ion-beam sputter deposition of ZnO films,” *J. Appl. Phys*., vol. 74, no. 1, pp. 244–248, 1993.
9. T. Tynell and M. Karppinen, “Atomic layer deposition of ZnO: A review,” *Semicond. Sci. Technol*., vol. 29, no. 4, p. 043 001, Feb. 2014.

DOI: https://doi.org/10.26799/cp-sict-plasmatech-tribology-2022

10. M. Leskelä, J. Niinistö, and M. Ritala, "Atomic layer deposition," in Comprehensive Materials Processing, S. Hashmi, G. F. Batalha, C. J. Van Tyne, and B. Yilbas, Eds., Oxford: Elsevier, 2014, pp. 101–123.
11. V. Rogé, et al., "Improvement of the photocatalytic degradation property of atomic layer deposited ZnO thin films: The interplay between film properties and functional performances," *J. Mater. Chem. A*, vol. 3, pp. 11 453–11 461, 21 2015.
12. R. Peter, et al., "Role of hydrogen-related defects in photocatalytic activity of ZnO films grown by atomic layer deposition," *J. Phys. Chem. C*, vol. 124, no. 16, pp. 8861–8868, 2020.
13. H. B. Profijt, S. E. Potts, M. C. M. van de Sanden, and W. M. M. Kessels, "Plasma-assisted atomic layer deposition: Basics, opportunities, and challenges," *J. Vac. Sci. Technol.*, vol. 29, no. 5, p. 050 801, 2011.
14. A. Omerzu, et al., "Large enhancement of photocatalytic activity in ZnO thin films grown by plasma-enhanced atomic layer deposition," *Surf. Interfaces*, vol. 23, p. 100 984, 2021.
15. M. Napari, M. Lahtinen, A. Veselov, J. Julin, E. Østreng, and T. Sajavaara, "Room-temperature plasma- enhanced atomic layer deposition of ZnO: Film growth dependence on the PEALD reactor configuration," *Surf. and Coat. Technol.*, vol. 326, pp. 281–290, 2017.
16. J. Pilz, et al., "Tuning of material properties of ZnO thin films grown by plasma- enhanced atomic layer deposition at room temperature," *J. Vac. Sci. Technol. A*, vol. 36, no. 1, 01A109, 2018.

Proceedings of the SICT/PlasmaTech/Tribology 2022 Joint International Conference
Barcelona, Spain – April 27 – 29, 2022
DOI: https://doi.org/10.26799/cp-sict-plasmatech-tribology-2022

Deposition of Microencapsulated Essential Oil from Neem Seeds on the Surface of Plasma-pretreated Cellulose Knitted Fabrics

Sanja Ercegović Ražić[1], Anja Ludaš[1*], Tihana Perinović[1]

[1] Department of Materials, Fibres and Textile Testing, University of Zagreb Faculty of Textile Technology و Prilaz baruna Filipovića 28a, Zagreb, Croatia, sanja.ercegovic@ttf.unizg.hr, anja.ludas@ttf.unizg.hr, tihana.perinovic@ttf.unizg.hr

Abstract

In this work, microencapsulation of neem essential oil (Azadirachta indica) was carried out by solvent evaporation technique. Cellulose knitted fabrics were treated with neem essential oil, which has a variety of antibacterial properties. Before treatment, the cellulose knitted fabrics were pretreated with oxygen and argon low pressure cold plasma under defined conditions. The synthesised microcapsules were applied to the textile material by a spray process. Surface analysis of the treated samples was carried out using a microscope FE-SEM, while microbiological tests were carried out using agar diffusion.

Keywords: neem essential oil, microencapsulation, plasma pretreatment, cellulose materials.

1. Introduction

Microencapsulation has proven to be a successful, environmentally friendly and economically viable technology for commercial application in the pharmaceutical and agrochemical industries and more recently in the textile industry [1, 2]. The microcapsule is the most effective way to store a substance as it allows controlled release of the active ingredient. The result of the microencapsulation process is called a "microcapsule". Such capsules are micro-sized and have a spherical or irregular shape. Microcapsules can be divided into two parts: core and shell. The core (inner part) contains the active ingredient (hardener, biocide, essential oil), while the shell (outer part) protects the core permanently or temporarily from the external atmosphere (Figure 1) [3-5]. An example are microcapsules containing essential oils, as friction occurs when wearing such textiles and active substances are then released. Essential oils are evaporable, natural and complex ingredients that are characterised by a strong odour. They come from aromatic plants and are secondary metabolic products [6]. The natural extract from the leaves of the plant neem has been used as an antimicrobial agent. Neem has broad-spectrum antibacterial activity against Gram-negative and Gram-positive microorganisms and also shows growth inhibitory activity against various pathogens, including bacteria, fungi and viruses [7-13].

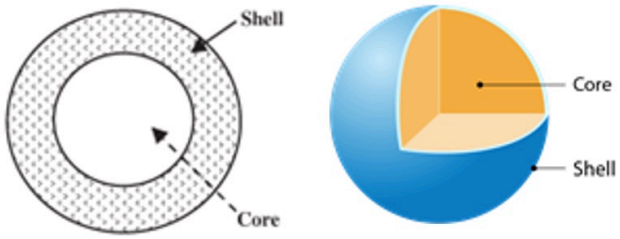

Fig. 1: Schematic representation of the microcapsule [14].

Due to the increasing environmental requirements imposed by modern textile technological processes, great importance is attached to environmentally friendly treatments. In the last two decades, a particular interest has been noted in the application of plasma technology in the textile field, especially in the pretreatment and finishing of textile materials to obtain multifunctional textile products. It is known that plasma treatment is primarily used for surface treatment of materials and plays an important role in modifying only the upper surface of the textile material down to a layer thickness of only a few tens of nanometres, leaving the basic (mechanical) properties almost unchanged [15-19].

2. Materials and Methods

The analyses were carried out on smooth, untreated knitted fabrics made of cotton and modal fibres (basis weight of 150 g/m2).

DOI: https://doi.org/10.26799/cp-sict-plasmatech-tribology-2022

Microencapsulation of neem (Azadirachta indica) essential oil was carried out by solvent evaporation. The microcapsules were synthesised according to the patent "NO: US 6,932,984 B1". The patent refers to the process of microencapsulation of cosmetic ingredients, vitamins, essential oils and pharmaceutical substances [2, 20]. Due to its diverse pharmacological and biological properties, the essential oil from neem seeds is used for the synthesis of microcapsules [7-13].

Before applying the synthesised microcapsules to textiles, cellulose knitted fabrics were pretreated with oxygen and argon low-pressure cold plasma under defined conditions to improve the adsorption and binding of the microcapsules to/on the structure of the textile material (Table 1).

Table 1: Oxygen and argon plasma pretreatment conditions.

Treatment conditions of installed plasma device	
Gas flow rate, q	200 cm^3/min
Power, P	500 W
Time of treatment, t	5 min
Initial (base) pressure, p	0.20 mbar
Working pressure, p	0.30 mbar

The synthesised microcapsules (MC) were applied to cotton and modal fibres by a spray method. The solution contains synthesised microcapsules in an amount of 30 g/l, 1,2,3,4-butanetetracarboxylic acid (BTCA) as binder in an amount of 20 g/l and distilled water. Using a sprayer (by Wurth), the microcapsules were applied to a knitted samples (diameter 13 cm). Uniform application of the microcapsule solution to the knitted fabric in the time of 10 s is possible because the ball bearing drive has a vortex effect. After application of the synthesised microcapsules, the material is fixed in the dryer at a temperature of 120 °C for 5 minutes.

The morphological analysis of the synthesised microcapsules was carried out with a field emission scanning electron microscope (FE-SEM, Tescan). Microbiological analysis of the samples for two bacteria (Staphylococcus aureus and Klebsiella pneumoniae) was performed using a qualitative agar diffusion test according to ISO 20645:2004 [21].

The procedure includes:

- Preparation of a bacterial inoculum of defined concentration (1-5-108 CFU (Colony Forming Unit)/mL)
- Inoculation of the bacteria on nutrient agar
- Preparation of a round textile sample (diameter 25 mm)
- Incubation of the textile samples on agar with bacterial meadow for a defined time (18-24 h) at a defined temperature (37 °C)
- Determination of antibacterial efficacy.

3. Results and Discussion

The microcapsules were synthesised according to the patent "NO: US 6,932,984 B1". The mass of the microcapsules obtained is approximately the same for each synthesis and is 0.320 g. The microcapsules are easily detached from the philtre paper after filtration and air drying, the weight of the microcapsules remaining on the philtre paper is very low, averaging 0.073 g, standard deviation (Figure 2).

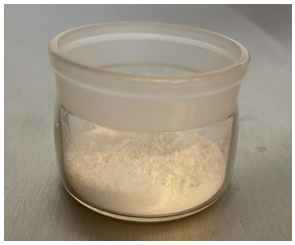

Fig. 2: Synthesised microcapsules with neem essential oil.

DOI: https://doi.org/10.26799/cp-sict-plasmatech-tribology-2022

SEM micro morphological analyses confirmed different shapes (mostly oval to circular) and sizes (approx. 1-80 μm) of the synthesised microcapsules. A porous cellulose shell protecting the contents of the microcapsule (neem essential oil) is also visible (Figure 3.).

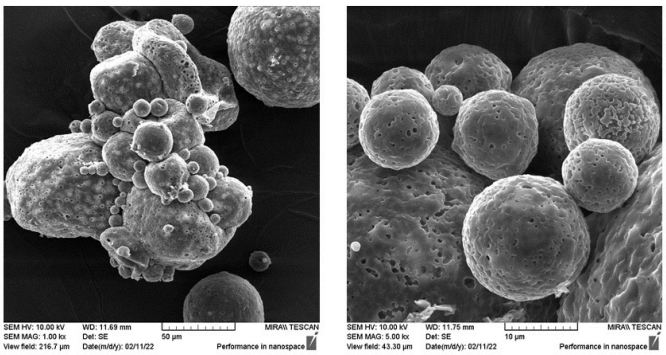

a) b)

Fig. 3: Synthesis of MC with neem essential oil, scanned with SEM microscope at 1000x and 5000x magnification.

The synthesised microcapsules were successfully sprayed onto the textile cellulose knitted material, which is also evident from the pictures from SEM. The microcapsules are evenly arranged along the surface of the cellulose fibres, with more or less agglomerates detaching with BTCA as the binder. (Figure 4. A2, b2, c2, d2, e2 and f2).

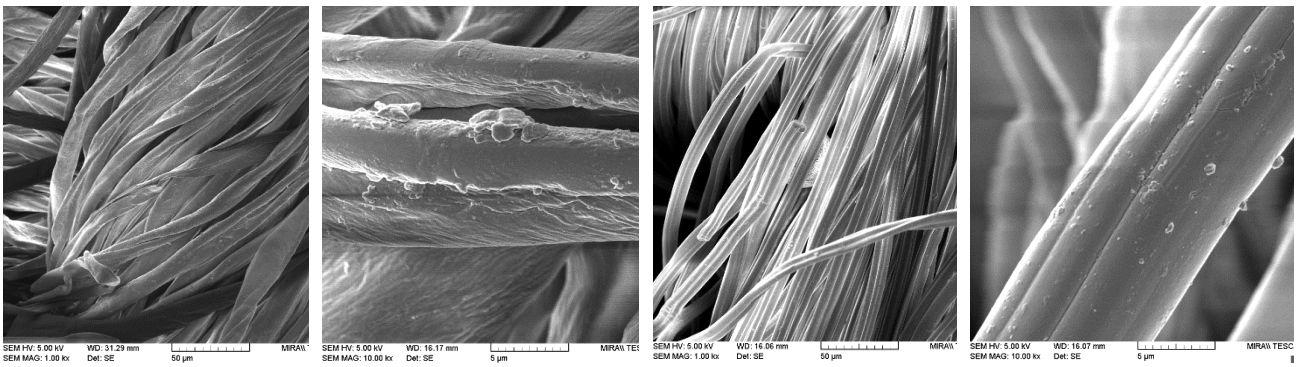

a1) cotton-untreated a2) cotton-untreated d1) modal-untreated d2) modal-untreated

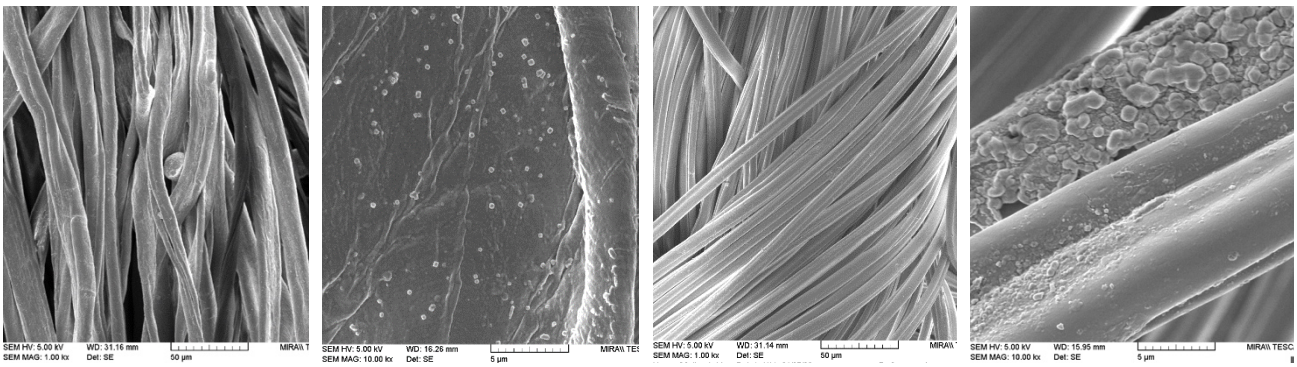

b1) cotton-O_2 plasma b2) cotton-O_2 plasma e1) modal-O_2 plasma e2) modal-O_2 plasma

DOI: https://doi.org/10.26799/cp-sict-plasmatech-tribology-2022

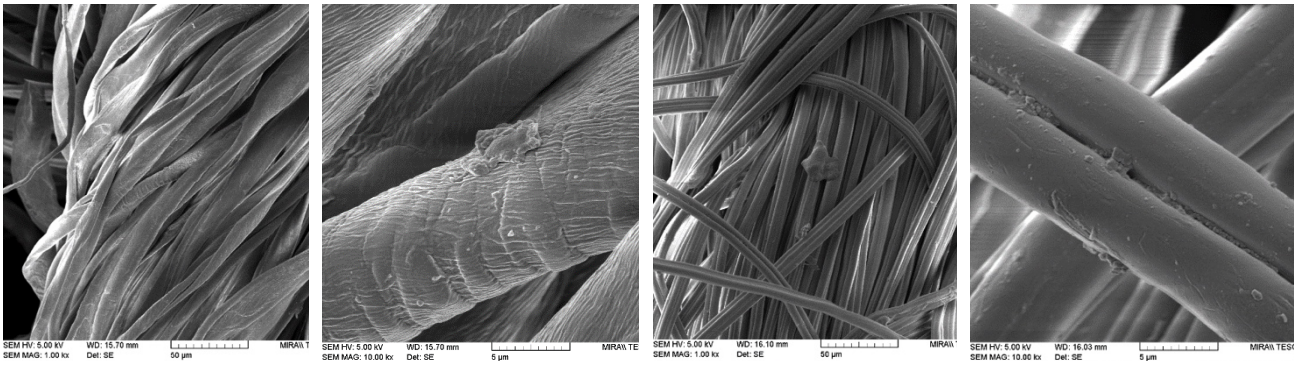

c1) cotton-Ar plasma c2) cotton-Ar plasma f1) modal-Ar plasma f2) modal-Ar plasma

Fig. 4: SEM Images of cellulose fibres to which microcapsules have been applied with and without plasma pretreatment, at 1000x and 10,000x magnification.

The synthesised microcapsules were better bound to the knitted fabric, the surface of which was pretreated with the environmentally friendly cold low-pressure plasma technology (O2, Ar).
Antimicrobial efficacy was tested on two bacterial species: Gram-positive Staphylococcus aureus and Gram-negative Klebsiella pneumoniae. For both samples (modal and cotton), the antimicrobial efficacy and reduction of bacterial growth among the samples is not evident using applied qualitative test (Figure 5.) The reason for these results could be that the neem oil is not exposed to the bacteria, which are enclosed in the microcapsules and protected by the shell. For this reason, a quantitative microbiological test should be carried out.

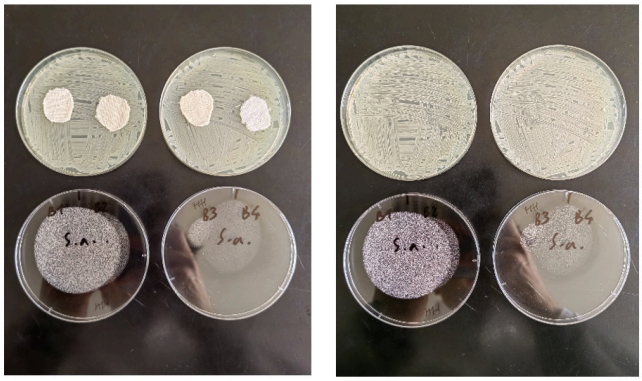

Fig. 5: Antimicrobial efficacy results

4. Conclusion

The proposed method for the synthesis of microcapsules seems to be acceptable as we obtained a good amount of microcapsules.

SEM The analysis confirms the morphology of the microcapsules with different sizes and shapes (from oval to circular); a porous cellulose shell is visible.

The synthesised microcapsules were successfully applied to the textile cellulosic materials (fibres) and better bonded to the knitted fabrics, whose surface was pretreated with environmentally friendly low-pressure plasma technology (O2, Ar).

The tested samples showed no antimicrobial activity against the two bacterial cultures. However, wearing such a material causes friction and the release of neem oil, which has an antibacterial effect [7-13].

Acknowledgements

This work was supported by the European Union through the European Social Fund under the project UP.03.1.1.04.0024 "Development and implementation of professional practise at the Faculty of Textile Technology". The Faculty of Textile Technology at the University of Zagreb is solely responsible for the content of the work.

DOI: https://doi.org/10.26799/cp-sict-plasmatech-tribology-2022

References

1. E. Adamowicz et al, "Microencapsulation of active substances and fragrances for use in textile materials," *Tekstil,* vol. 64, no. (3-4), pp. 122-127, 2015.
2. I. Brlek, A. Ludaš, A. Sutlović, "Synthesis and Spectrophotometric Analysis of Microcapsules Containing Immortelle Essential Oil," *Molecules*, vol. 26, no. 8, pp. 1-9, 2021.
3. B. Boh and E. Knez, "Microencapsulation of essential oils and phase change materials for applications in textile products," *Indian journal of fibre & textile research*, vol. 31, pp. 72-82, 2006.
4. I. Matijević, T. Pušić, S. Bischof, "Cosmetic preparations on textiles: cosmetotextiles," *Tekstil*, vol. 65, no. 1-2, pp. 1-12, 2016.
5. A. J. West and K. E. Aruiett-Hitchcock, "A Critical Review of Aroma Therapeutic Applications for Textiles," *Journal of Textile and Apparel Technology and Management*, vol. 9, no. 1, pp. 1-13, 2014.
6. F. Bakkali et al, "Biological effects of essential oils-A review," *Food and Chemical Toxicology*: *An International Journal Published for the British Industrial Biological Research Association*, vol. 46, no. 2, pp. 446-475, 2008.
7. K. Biswas et al, "Biological activities and medicinal properties of neem (Azadirachta indica)," *Current science*, vol. 82, no. 11, pp. 1336-1346, 2002.
8. A. Eid, N. Jaradat, N. Elmarzugi, "A Review of chemical constituents and traditional usage of Neem plant (Azadirachta indica)," *Palestinian Medical and Pharmaceutical Journal*, vol. 2, no. 2, pp. 75-81, 2017.
9. M. M. Sadeghian and F. Mortazaienezhad, "Investigation of Compounds from Azadirachta indica (Neem)," *Asian Journal of Plant Sciences*, vol. 6, no. 2, pp. 444-445, 2007.
10. V. S. Kumar, V. Navaratnam, V., "Neem (Azadirachta indica): Prehistory to contemporary medicinal uses to humankind," *Asian Pacific Journal of Tropical Biomedicine,* vol. 3, no. 7, pp. 505-514, 2013.
11. N. A. Farooqui et al, "Antibacterial potential of nimbolide from Azadirachta indica," *International Journal of Pharmacy and Pharmaceutical Sciences*, vol. 6, no. 5, pp. 636-638, 2014.
12. K. Saranya et al, "Evaluation of Radiation Absorption Capacity of Azadirachta Indica," *International Journal for Research in Applied Science & Engineering Technology*, vol. 7, no. 9, pp. 31-33, 2019.
13. M. Hasan et al, "Impact of neem in case of antimicrobial activity on single jersey cotton fabric," *International Journal of Textile and Fashion Technology*, vol. 8, no. 4, pp. 1-6, 2018.
14. S. K. Ghosh, "Functional Coatings and Microencapsulation: A General Perspective," in *Functional Coatings*, WILEY-VCH Verlag GmbH & Co. KGaA, pp. 1-26, 2006.
15. S. Ercegović Ražić and R. Čunko, "Modification of Textile Properties Using Plasma," *Tekstil*, vol. 58, no. 3, pp. 55-74, 2009.
16. B. Kutlu and A. Cireli, "Plasma technology in textile processing," Dokuz Eylul University, Textile Engineering Department, 35100, Bornova-IZMIR, 2016.
17. R. Shishoo, "Plasma technologies for textiles," Published by Woodhead Publishing Limited in association with Textile Institute, Abington Hall, Cambridge, England, 2007.
18. J. Peran and S. Ercegović Ražić, "Application of atmospheric pressure plasma technology for textile surface modification," *Textile Research Journal*, vol. 90, no. 9-10, pp. 1174-1197, 2020.
19. S. Ercegović Ražić et al,"Application of AFM for identification of fibre surface changes after plasma treatments," *Materials Technology*, vol. 26, no. 3, pp. 146-152, 2011.
20. V. Babtsov, Y. Shapiro, E. Kvitnitsky, "Method of Microencapsulation," U.S. Patent 6,932,984 B1, 2005.
21. ISO 20645:2004 Standard*:* a method for the determination of the effect of antibacterial treatments applied to woven, knitted and other flat textiles.